

Half-wave nanolasers and intracellular plasmonic lasing particles

Received: 2 April 2024

Accepted: 27 November 2024

Published online: 02 January 2025

 Check for updates

Sangyeon Cho ^{1,2}, Nicola Martino ^{1,2} & Seok-Hyun Yun ^{1,2,3} 

The ultimate limit for laser miniaturization would be achieving lasing action in the lowest-order cavity mode within a device volume of $\leq(\lambda/2n)^3$, where λ is the free-space wavelength and n is the refractive index. Here we highlight the equivalence of localized surface plasmons and surface plasmon polaritons within resonant systems, introducing nanolasers that oscillate in the lowest-order localized surface plasmon or, equivalently, half-cycle surface plasmon polariton. These diffraction-limited single-mode emitters, ranging in size from 170 to 280 nm, harness strong coupling between gold and $\text{In}_x\text{Ga}_{1-x}\text{As}_{1-y}\text{P}_y$ in the near-infrared ($\lambda = 1,000\text{--}1,460$ nm), away from the surface plasmon frequency. This configuration supports only the lowest-order dipolar mode within the semiconductor's broad gain bandwidth. A quasi-continuous-level semiconductor laser model explains the lasing dynamics under optical pumping. In addition, we fabricate isolated gold-coated semiconductor discs and demonstrate higher-order lasing within live biological cells. These plasmonic nanolasers hold promise for multi-colour imaging and optical barcoding in cellular applications.


Every resonant system has its fundamental oscillation frequency, at which the entire resonator precisely contains the half-wave of oscillation (or the quarter-wave for asymmetric resonators). Most electrical, acoustical and mechanical oscillators typically operate at these fundamental frequencies. In an optical laser, the fundamental oscillation corresponds to a mode with a wavelength (λ) that is equal to half (or a quarter) of the resonator's length divided by its refractive index (n). However, all previously demonstrated lasers have operated in higher-order modes or with multi-wavelength-sized resonators. For a given wavelength, the smallest laser size would be achieved using the fundamental half-wave mode.

Photonic lasers that incorporate periodic reflections into the cavity, such as distributed feedback lasers¹, photonic crystal lasers^{2,3} and moiré lattice lasers^{4,5}, achieve a high-quality-factor (high- Q) Bragg reflection and routinely operate with their lowest-order photonic cavity modes. However, although these modes, which are formed via the coupling of a central defect core mode with the stop band of a periodic crystal structure or Bloch mode coupling induced by moiré reciprocal lattice vectors^{4,5}, could have near-diffraction-limited mode volumes, their electric fields extend multiple half-wavelengths into the periodic structures, requiring multi-wavelength device sizes.

Metallic reflectors have proved to be useful for laser miniaturization. Notably, the lasing of an HE_{11} -like mode at a cryogenic temperature (77 K) has been achieved in a metal-coated Fabry–Pérot (FP) pillar laser with a diameter of 260 nm and a height of approximately 500 nm (ref. 6). In addition, an FP cavity with metallic end-mirrors, measuring 406 nm in diameter and 230 nm in height, achieved lasing of a transverse magnetic TM_{111} -like mode under cryogenic conditions⁷. However, whereas these modes represent the lowest 'photonic like' modes, they are not the fundamental modes, as the metal-incorporated structures support plasmonic modes of lower orders along the metal–semiconductor interfaces.

The tight binding of photons and plasmons, or plasmon polaritons⁸, offers a promising approach for developing small lasers when their volumes approach the diffraction limit, where photonic modes cannot be confined. Surface plasmon polaritons (SPPs) facilitate achieving subwavelength mode volumes (V_m), which, through the Purcell effect, enable higher gain extraction from gain media. Since the initial demonstrations of plasmonic lasing^{6,9,10}, numerous avenues have been explored^{11–22}. However, whereas the transverse dimensions of these lasers are typically at a subwavelength scale, their longitudinal mode order has not yet reached the fundamental limit. Resonator

¹Wellman Center for Photomedicine, Massachusetts General Hospital, Cambridge, MA, USA. ²Harvard Medical School, Boston, MA, USA.

³Harvard–MIT Health Sciences and Technology, Cambridge, MA, USA.  e-mail: syun@hms.harvard.edu

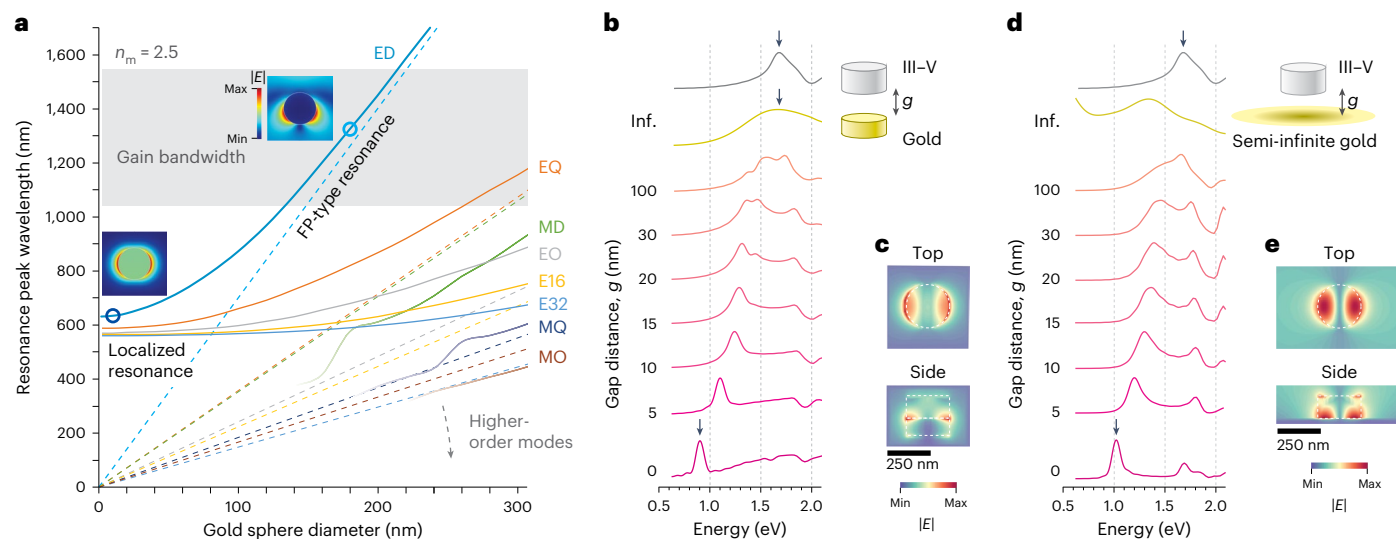


Fig. 1 | Strong coupling of plasmonic and semiconductor dipolar modes. **a**, Theoretical peak wavelengths for different resonance modes at various diameters of the gold sphere in an environment with a refractive index of 2.5. The solid curves represent gold, whereas the dashed curves are for a perfect conductor with an infinite plasma frequency. For the ED mode, the insets show the electric field amplitude ($|E|$) profiles in the quasi-static (left) and dynamic (right) regimes, where the colour scale applies to both profiles. In the FP regime, only the ED mode can be placed within the gain bandwidth, excluding all higher-order modes. **b**, Simulated Mie scattering spectra of a complex comprising a

III–V semiconductor ($n = 3.5$) and a gold nanodisc, with a diameter of 250 nm (both) and a height of 130 nm (semiconductor) and 100 nm (gold), for various gap distance (g) values. The arrow indicates the lowest-order mode at contact. Inf., infinite distance. **c**, Top and side views of the electric field amplitude profiles of the semiconductor–gold particles in contact (dashed outline). **d**, Simulated Mie scattering spectra of a semiconductor nanodisc ($n = 3.5$) on a flat gold substrate for different gap distances. The arrow indicates the lowest-order mode at contact. **e**, Top and side views of the electric field amplitude profiles of the semiconductor-on-gold structure (outlined with the dashed line).

lengths longer than the half-wavelength, $\lambda/2n$, have commonly been used to take advantage of the extended amplification length and higher quality factors of the higher-order modes. The concept of surface plasmon amplification by stimulated emission of radiation (or spaser)²³ has prompted considerable interest, but the convincing experimental realization of a deep-subwavelength spaser has remained elusive^{24–26}. The lowest plasmonic mode order ever demonstrated was second-order from coaxial¹³ and nanorod²⁷ lasers, both at cryogenic temperature.

Here we report our observation of the fundamental mode oscillation from half-wavelength nanolasers at room temperature. Our laser consists of a III–V semiconductor particle, as small as 190 nm in lateral size and 130 nm in thickness for $\lambda = 1,190$ nm, on a gold substrate^{28,29}. We describe the key design principles and operation in the near-infrared (NIR). In addition, moving away from the substrate-based design, we develop substrate-free plasmonic laser particles. Using submicrometre particles which emit single peaks that are tunable across a wide spectral range, we demonstrate plasmonic lasing within live cells.

Design of half-wave laser

The challenges for previous attempts at nanoscale spasers based on localized surface plasmons (LSPs)^{24,25,30} can be understood through a simple gain–loss analysis. To reach the lasing threshold, the theoretical minimum pumping rate required is $M\omega/Q$, where M denotes the number of modes over which the pump energy is distributed, ω is the optical frequency and Q is the cavity quality factor. At least $\omega\tau_s/Q$ gain emitters are needed to absorb the pump energy, where τ_s is the spontaneous radiative lifetime, modified from its free-space value τ_0 by a Purcell factor:

$$F_p = \frac{3}{4\pi^2} \frac{Q}{V_m} \left(\frac{\lambda}{n}\right)^3 \quad (1)$$

When the gain bandwidth ($\Delta\omega$) is broader than the cavity bandwidth (ω/Q), the minimal emitter density (ρ_{\min}) must exceed $\sim \frac{\Delta\omega\tau_0}{Q} \left(\frac{\lambda}{2n}\right)^3$ (Supplementary Note 1). For instance, for a single-mode ($M = 1$) resonator

with $\Delta\omega = 3 \times 10^{14}$ Hz, $\tau_0 = 10^{-9}$ s, $\lambda/2n = 180$ nm and $Q = 10$, ρ_{\min} is approximately 5×10^{18} cm⁻³. Achieving this density with fluorophores or quantum dots without substantial non-radiative quenching is challenging³¹. Moreover, deep-subwavelength metallic nanospheres would require a greater pump energy due to their large M (>40), which could lead to excessive heating³².

Our strategy focuses on avoiding non-radiative coupling to higher-order plasmonic modes by operating in the NIR region, away from the surface plasmon frequency (ω_{sp}), to achieve $M = 1$. In addition, we aim for high gain from bulk III–V semiconductors driven substantially above their bandgap. This principle is applicable to various semiconductor–metal particle structures. For instance, consider a gold sphere immersed in a medium with an effective refractive index (n_m) of 2.5. Figure 1a shows the resonance wavelengths of various plasmonic modes³³. For deep-subwavelength values of the particle diameter (d), the electric dipole (ED) and higher-order modes (that is, electric quadrupole (EQ), electric octupole (EO), E16 and E32) converge near 600 nm, corresponding to LSP resonances near ω_{sp} . As the diameter exceeds the quasi-static limit, the resonance curves shift due to phase retardation³⁴. Beyond this transition, the magnetic modes (that is, magnetic dipole (MD), magnetic quadrupole (MQ) and magnetic octupole (MO)) develop, and both electric and magnetic modes follow linear dispersion curves. Besides this LSP picture, the dispersion can be explained from the perspective of SPP waves. Further away from ω_{sp} , the refractive index of the SPP wave approaches n_m . The asymptotic line for the ED corresponds to the half-wavelength FP resonance given by $\lambda \approx 2.81n_m d$, whereas EQ has a slope of $\lambda \approx 1.41n_m d$, and so on (Supplementary Note 4)³⁵. Near ω_{sp} , the SPP wavelength is significantly reduced, causing the dispersion curves to bend. In this context, the LSP can be viewed as the half-wave resonance of the SPP near ω_{sp} , and previous nanolasers that utilized higher-order SPP waves can be interpreted as the lasing of multipole LSP modes in the FP regime. An important insight gained is that whereas the ED is spectrally close to other modes in the quasi-static regime, modal separation increases in the FP regime, allowing only the lowest-order mode to fall within the wide bandwidth of a gain medium (Extended Data Fig. 1a–c).

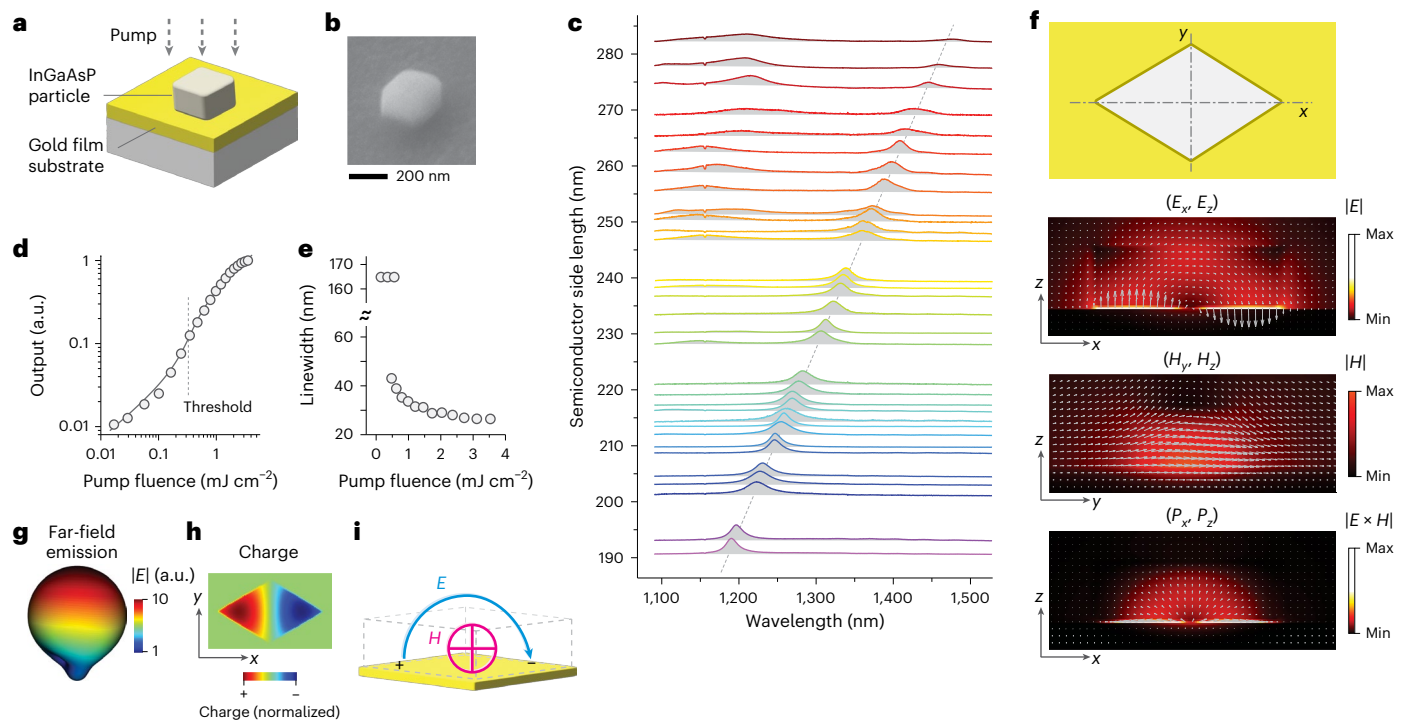


Fig. 2 | Characteristics of semiconductor-on-gold nanodevices. **a**, Schematic of the semiconductor-on-gold design. **b**, Scanning electron microscopy (SEM) image of an $\text{In}_{0.53}\text{Ga}_{0.47}\text{As}_{0.92}\text{P}_{0.08}$ particle with a side length of 170 nm (280 nm from corner to corner) and a height of 130 nm. **c**, Emission spectra from particles of different sizes, with the dotted line indicating the FDTD-derived tuning curve. **d**, Measured light–light curve (circle symbols) of a sample, with the theoretical

fit shown by the solid curve ($\beta = 0.06$). **e**, Measured linewidth at different pump fluences. **f**, Top to bottom: top-view schematic of the half-wave device, and the electromagnetic fields in an x – z cross-section of the mid plane for the electric field (E), magnetic field (H) and Poynting vector ($P = E \times H$). **g**, Computed far-field emission pattern. **h**, Induced charges ($\nabla \cdot E$). **i**, Schematic of the lowest-order MD mode.

The same principle applies to gold nanodiscs, to which III–V semiconductor discs are attached. Figure 1b depicts the Mie scattering spectra of a gold disc (diameter (D), 250 nm; thickness, 100 nm) and a semiconductor disc with a refractive index of 3.5, with an identical diameter and a thickness of 130 nm. When the two discs are well separated, each exhibits its fundamental dipolar mode at 1.69 eV ($\lambda = 730$ nm). As the two discs are brought closer, their modes increasingly couple, and the lowest-order hybrid mode emerges at 0.9 eV (1,380 nm) upon contact. This fundamental mode localizes at the metal–semiconductor interface (Fig. 1c). Our finite-difference time-domain (FDTD) analysis demonstrates that the strong mode coupling results in a cavity Q of up to 20. Strong coupling is also observed when the gold disc is replaced by an oversized substrate (Fig. 1d,e and Extended Data Fig. 1d), with $Q \approx 10$. Similar mode coupling is observed with non-circular shapes³⁶, such as rectangles and rhombi (Extended Data Fig. 1e–i).

Laser experiment and modelling

We fabricated particles of $\text{In}_{0.53}\text{Ga}_{0.47}\text{As}_{0.92}\text{P}_{0.08}$ semiconductor using both dry and wet etching (Extended Data Fig. 2). By controlling the etching time, we achieved rhombus-like particles ranging from 100 and 300 nm in size and with a thickness of 130 nm. They were placed on a high-quality polycrystalline gold substrate manufactured using a template-stripping method²⁹ (Fig. 2a). We used a 1,064 nm pump laser (2.5 MHz repetition and 2 ns pulse width) and a grating-based InGaAs camera spectrometer (0.8 nm resolution) (Extended Data Fig. 3a). Figure 2c displays the emission spectra collected from 32 particles at pump fluences of ~ 2 mJ cm⁻². The spectra are arranged along a theoretical tuning slope described by $\lambda = 3.09L + 596$ (nm), where L represents the side length of the rhombus. Particles smaller than 250 nm exhibit single emission peaks at wavelengths as short as $\sim 1,200$ nm (the bandgap is near 1,570 nm). For larger particles, second peaks are observed, which are attributed to dipolar modes oriented along the shorter axes

of the particles. We also conducted experiments with InGaAsP particles coated with a 5-nm-thick insulating layer of silica (SiO_2) and obtained similar results. This is probably due to the surface roughness of the particles, which provided an insulating air space.

As the pump fluence was varied, each particle showed a nonlinear growth in intensity, linewidth narrowing and a single-polarization spectral peak over a quasi-unpolarized background (Extended Data Fig. 3). For instance, at room temperature, one device with a size of about 245 nm displayed a threshold at $350 \mu\text{J cm}^{-2}$ with a fitted spontaneous emission factor (β) of 0.06 (Fig. 2d). Across the threshold, abrupt spectral narrowing was observed (Fig. 2e). The linewidth of the lasing mode was 45 nm at the threshold but decreased to 27 nm at higher pump powers (Extended Data Fig. 3b–d).

In the FDTD simulation, only one resonance mode was found within the broad fluorescence bandwidth. Its electromagnetic field is strongest near the metal plane, with the electric field primarily oriented perpendicular to the metal surface. Within the semiconductor, the electric field forms a loop from one side to the other, encircling the magnetic field, which oscillates along the minor axis. This configuration results in radial energy radiation (leakage) from the metal–semiconductor laser (Fig. 2f and Supplementary Fig. 3). The far-field emission can be efficiently collected in the vertical direction (Fig. 2g). With a dipolar charge distribution (Fig. 2h), this half-wave mode corresponds to an MD mode (Fig. 2i). It is important to note that a similar MD mode is the lowest mode in cylindrical dielectric resonators³⁷, whereas spheres exhibit an ED mode as the lowest. In our geometry, with the metal surface acting as a mirror, the MD mode can be interpreted as an ED mode in a flattened coordinate system (with the polar angle mapped to the x axis and the azimuthal angle to the y axis) or as the lowest-order Mie-like transverse magnetic (or TM) mode³⁷.

Building on a standard semiconductor laser model (Fig. 3a), we formulated quasi-continuous-level rate equations in the spectral

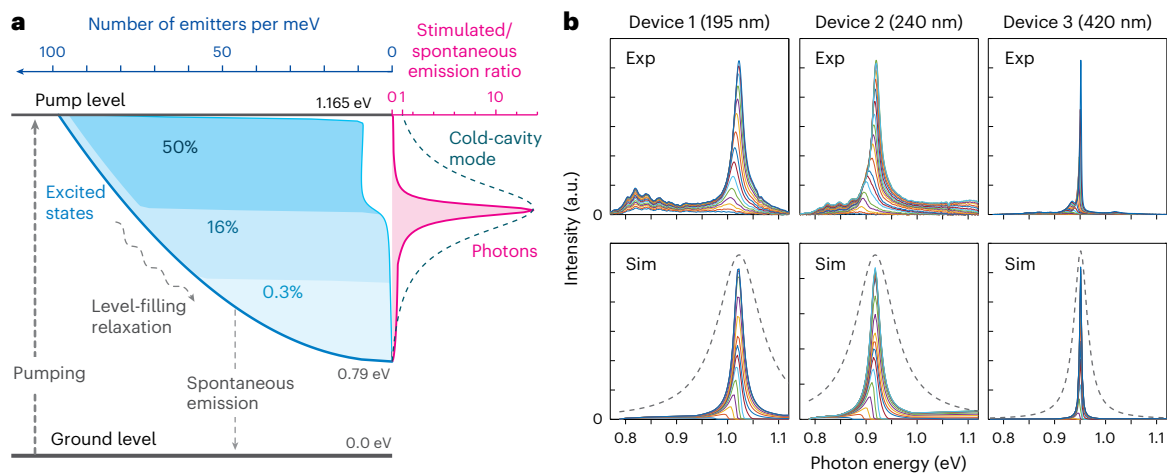


Fig. 3 | A semiconductor laser ‘waterfall’ model. a, Energy diagram of gain emitters (electron–hole pairs) and photons (polaritons) in a cavity. The dashed curve represents the Lorentzian mode profile below the laser threshold. The population in the excited states (bluish shades) and the output spectrum (cyan) are illustrated for a 240-nm-diameter device at a pump fluence of 0.8 mJ cm^{-2} . At the beginning of the pump pulse (0.3% of the total pump energy), only the bottom excited states are filled. As the pump increases (to 16%), the quasi-Fermi level elevates to the mode centre frequency at which the threshold has been reached. At the peak of the pump pulse (50% energy), stimulated emission exceeds spontaneous emission near the centre of the cold-cavity-mode spectrum

domain (Methods and Supplementary Note 3). The model did not consider any expected spatial dependence in the spontaneous and stimulated emission rates, nor the accompanying depletion and diffusion³⁸ of electron–hole pairs, treating them as spatially averaged parameters. Given the bandgap edge at 1,570 nm and optical pumping at 1,064 nm, the total number of gain emitters available is estimated to be $\sim 1 \times 10^{19} \text{ cm}^{-3}$. This large carrier concentration is normally not achievable due to Auger recombination ($\sim 2.3 \times 10^{-29} \text{ cm}^6 \text{ s}^{-1}$ for InGaAsP), but is attained in plasmonic cavities due to enhanced radiative emission. Within the mode bandwidth $\Delta\Omega (= \omega/Q)$ centred at 1,240 nm, the number of gain emitters is $3.4 \times 10^{18} \text{ cm}^{-3}$ for $Q = 10$. In a bulk semiconductor, the theoretical maximum free-space gain would be around $3,000 \text{ cm}^{-1}$ at 1,240 nm, which is insufficient to compensate for the cavity loss ($2n\pi/\lambda Q$) of $\sim 17,700 \text{ cm}^{-1}$ (Supplementary Note 2). The gain enhancement provided by the Purcell factor F_p for subwavelength modes makes it possible to reach the threshold (Extended Data Fig. 4).

Remarkably, our numerical simulation closely reproduced the experimental results. Figure 3b illustrates the measured and simulated spectra of two half-wave devices and a one-wave device. At low pump power values, only spontaneous emission near the band edge is evident. As the pump power is increased, the excited band fills up, and the spontaneous emission peak shifts towards higher energies. With stronger pumping, photons (polaritons) accumulate in the cavity and, eventually, stimulated emission surpasses spontaneous emission within the mode’s spectral bandwidth. On reaching this threshold, the linewidth decreases and the number of output photons increases nonlinearly (Extended Data Fig. 5). A kink, characteristic of a small spontaneous emission factor ($\beta \ll 1$), appears even when only one mode is present in the gain bandwidth. This apparent kink in the light-in–light-out curve results from level-filling; the amplification of the mode must wait until the quasi-Fermi level of the emitter energy reaches the mode resonance. The so-called threshold-less lasing is not possible in this case. The roll-off of the output power at higher pump levels can be attributed to increasing non-radiative Auger recombination. Ultimately, the output saturates when all excited states have been populated.

(dashed curve). See Extended Data Fig. 4 and Supplementary Note 3 for more details. **b**, Comparison of experimental (Exp) and simulation (Sim) spectra for two lowest-order devices (device 1 (195 nm diameter) and device 2 (240 nm), both with $Q = 10$ and $F_p = 18$) and one higher-order device (device 3 (420 nm), $Q = 30$ and $F_p = 8$) across a pump fluence range of $0.03\text{--}3 \text{ mJ cm}^{-2}$. Different colours represent different pump fluences. Dashed grey curves represent cold-cavity mode profiles used in simulations. A periodic spectral fringe appears between 0.8 and 0.88 eV due to internal optical interference within a dichroic filter in the set-up. See Extended Data Fig. 5 for the light-in–light-out curves and linewidths.

Temporal and spatial characteristics of laser output

We compared particles on a gold substrate (plasmonic devices) with those on SiO_2 -coated silicon substrates (dielectric or photonic devices). A total of 120 devices, produced from six batches of plasmonic devices and two batches of photonic devices, were examined, each with different average particle sizes but similar thicknesses, around 290 nm (Fig. 4a and Extended Data Fig. 6). As the particle size and oscillating mode order were increased, the lasing threshold showed a modest decrease (Fig. 4b), whereas the linewidth narrowed significantly to 4–6 nm. For dielectric devices, lasing was observed only for particle sizes larger than 880 nm, even at the highest pump fluence of 8 mJ cm^{-2} (refs. 28,29,39). Under picosecond pumping ($\sim 70 \text{ ps}$) with a seed-amplified laser (765 nm, 2.5 MHz), these devices required a fraction of the peak threshold power compared with nanosecond pumping (2 ns) (Extended Data Fig. 6d), primarily due to the accelerated carrier lifetime of charge carriers by the Purcell effect. Using picosecond pumping and a single-photon InGaAs avalanche photodiode, we measured the fluorescence decay time of half-wave devices to be well below the instrument’s resolution of 140 ps, a substantial reduction from the 1–2 ns decay time observed in pristine bulk wafers at the same pump intensities (Extended Data Fig. 7). The finite resolution prevented us from capturing theoretically expected changes in temporal profiles across the lasing threshold for the half-wave devices. For larger devices, however, resolution-limited temporal narrowing was clearly observed (Extended Data Fig. 7).

To investigate far-field emission profiles, we used $\text{In}_{0.8}\text{Ga}_{0.2}\text{As}_{0.44}\text{P}_{0.56}$ semiconductor particles and achieved half-wave lasing in the 1,000–1,100 nm spectral range, which falls within the extended detection range of silicon cameras that are available to us. Under picosecond pumping, rhombus-shaped particles with a side length of between 150 and 200 nm and a thickness of 200 nm exhibited narrowband lasing emission with linewidths as narrow as 6 nm (Fig. 4c), with a distinct threshold at approximately 1 mJ cm^{-2} (Fig. 4d). FDTD simulations indicated that these samples support the half-wave mode in this spectral range, with Q factors of 10–13. The high lasing Q factor of 170 is probably due to the increased gain of this InGaAsP composition³⁸

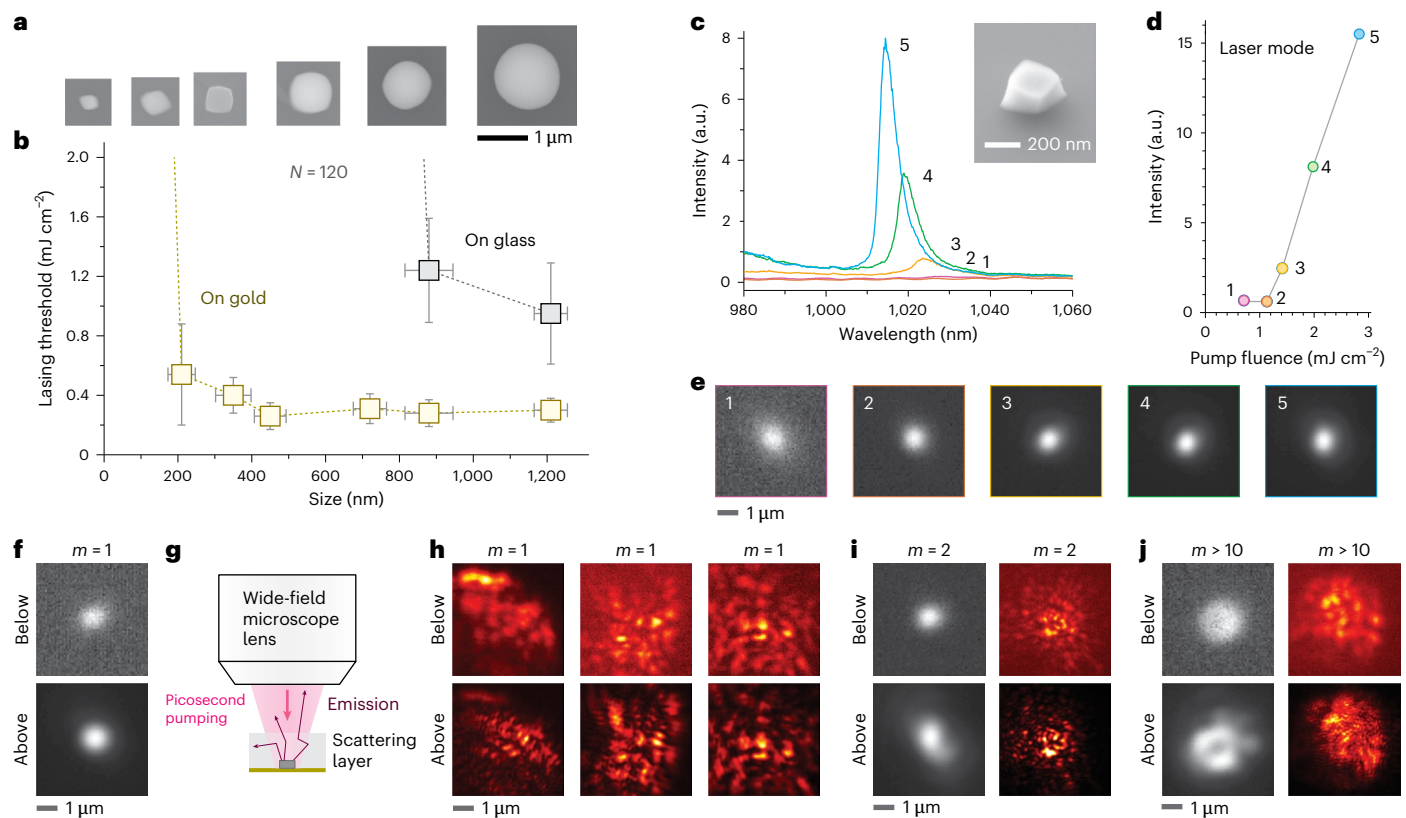


Fig. 4 | Dependence of lasing threshold and far-field emission on particle size.

a, SEM images of representative $\text{In}_{0.53}\text{Ga}_{0.47}\text{As}_{0.92}\text{P}_{0.08}$ samples from different fabrication batches, each with various semiconductor sizes. **b**, Measured laser thresholds for different sample batches on gold (yellow) and glass (grey) substrates. The total sample number (N) is 120, with 15 samples per batch. Data points (squares) represent the mean values, and the error bars (horizontal and vertical) indicate the standard deviation. The batch with a mean size of 200 nm corresponds to lowest-order half-wave devices, whereas the data point at 350 nm reflects the devices operating in second-order modes. **c**, Emission spectra of a representative $\text{In}_{0.80}\text{Ga}_{0.20}\text{As}_{0.44}\text{P}_{0.56}$ half-wave device (mode order (m) = 1) in the 1,000–1,100 nm range at various pump fluences. Inset: SEM image of a

representative particle with a size of 170 nm and a height of 200 nm.

d, Light-in–light-out data corresponding to the spectra in **c**. **e**, Far-field emission patterns of the half-wave device according to the pump fluences in **c**. **f**, Far-field emission patterns of another half-wave device below and above the threshold. **g**, Schematic of the set-up for imaging the output emission from a device embedded beneath a scattering matrix (80- μm -thick Scotch tape). **h**, Speckle images from three different half-wave devices below and above the threshold. **i**, Far-field emission patterns from a second-order device ($m = 2$) without (left) and with (right) a scattering matrix. **j**, Far-field patterns from a higher-order-mode ($m > 10$) device without (left) and with (right) a scattering matrix.

and the greater pump absorption (producing more carrier charges) with 765 nm light compared with 1,064 nm.

The optical emission images of the half-wave devices showed circular, near-diffraction-limited patterns (Fig. 4e,f). By contrast, higher-order-mode devices displayed whispering-gallery-mode patterns above the lasing threshold (Fig. 4i,j). Moreover, to simulate intra-tissue imaging we covered the devices with translucent tape (3M Scotch Magic tape, 80- μm -thick) and measured the emission through the scattering matrix (Fig. 4g)⁴⁰. As shown in Fig. 4h, the speckle patterns became more vivid above the threshold due to the narrower and spatially coherent laser emission. Higher-order-mode devices exhibited more distinct changes at the threshold (Fig. 4i,j).

Plasmonic laser particles for cell barcoding

In previous work, photonic laser particles based on InGaAsP microdisks have been developed and their applications demonstrated in single-cell analyses, such as cell tracking, imaging and flow cytometry^{41–43}. Miniaturized laser particles are desirable for these applications, as well as super-resolution imaging⁴⁴ and sensing⁴⁵, as they cause minimal perturbation⁴², which is especially valuable in the NIR range outside the conventional 400–800 nm window used for fluorescence measurements.

To create metal–semiconductor laser particles, we coated $\text{In}_{0.73}\text{Ga}_{0.27}\text{As}_{0.58}\text{P}_{0.42}$ pillars in situ on a wafer with an SiO_2 layer, followed

by the deposition of a gold layer on top via evaporation (Fig. 5a). Electron microscopy revealed a conformal gold coating of 80–100 nm thickness found exclusively on one side (Fig. 5b and Extended Data Fig. 8), with a 5-nm-thick insulating layer of SiO_2 between the semiconductor and the gold (Fig. 5c and Extended Data Fig. 8). Unlike earlier substrate-based devices, the gold–InGaAsP particles with half-wavelength sizes did not reach the lasing threshold. We attributed this to the lower quality of the gold layers formed (Extended Data Fig. 9a), although this can be improved⁴⁶. The smallest laser particle batch that exhibits lasing in air had a size of 580 nm (Fig. 5d), corresponding to a longitudinal mode order of 3. This size is two or three times smaller than typical non-gold-coated InGaAsP laser particles in the same spectral range. Under nanosecond pumping (1,064 nm, 2 MHz), the measured emission linewidths were below 4 nm, indicating linewidth Q factors of over 250, suitable for spectral multiplexing and barcoding.

In addition, we coated the gold-deposited InGaAsP particles with a 60-nm-thick layer of SiO_2 to enhance both the material and optical stability in aqueous environments. Figure 5e presents the laser spectra from 31 SiO_2 -coated laser particles in water, with diameter values ranging from 780 to 920 nm. The single-mode tuning range extends up to 150 nm and can be expanded further using different InGaAsP compositions. These particles operate in whispering gallery modes (Fig. 5f). Similar narrowband lasing was also observed from laser particles with

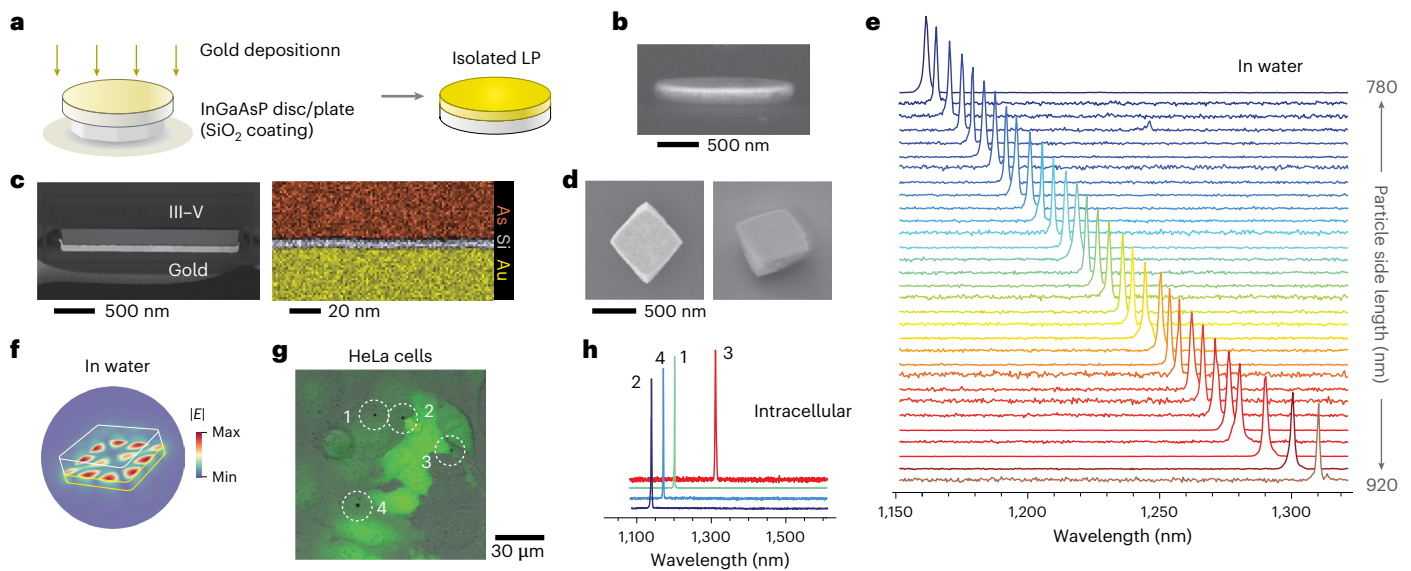


Fig. 5 | Plasmonic laser particles and intracellular lasing. **a**, Schematic showing fabrication of the laser particles. LP, laser particle. **b**, Electron micrograph of an isolated particle. **c**, Elemental analysis images of a gold–semiconductor particle. **d**, SEM images of 580 nm samples. **e**, Output spectra of 31 laser particles in water over a wide wavelength range with pumping at $-20 \text{ pJ } \mu\text{m}^{-2}$ per pulse.

f, FDTD simulation of a lasing mode in water. **g**, Microscope image of HeLa cells (expressing green fluorescent protein) tagged with gold-deposited laser particles (1 to 4, indicated by the dashed circles). **h**, Spectra measured from the intracellular plasmonic nanolasers marked in **g**.

a thinner gold thickness of 15 nm, enabling optical pumping through the gold (Extended Data Fig. 8).

For cell tagging and biocompatibility, we functionalized the SiO_2 -coated laser particles with a polyethyleneimine coating. After incubation with HeLa cells, the polymer-coated laser particles were internalized into the cytoplasm (Fig. 5g). With optical pumping, these intracellular lasers generated a linewidth of 4 nm (Fig. 5h). A pump energy of several picojoules per pulse and a peak power of less than 1 mW are acceptable for biological applications, especially when the pump beam can be rapidly scanned across cells in imaging or flow instruments⁴⁷. No detrimental effects of the laser particles on cell viability were observed. Using conventional photonic laser particles coated with the same polymers, we have observed minimal effects of the intracellular laser particles on cell division, surface receptors and transcriptomic phenotypes^{41–43}. The presence of gold within the polymer layer would not affect the biocompatibility.

Conclusions

Our work has successfully demonstrated lasers operating at fundamental oscillation frequencies by harnessing the half-wave dipolar plasmonic mode. This achievement enables smaller device sizes compared with previous higher-order devices, even outperforming those operating at cryogenic temperatures (see Extended Data Fig. 10). The miniaturization approach may prove useful for developing high-density light-source arrays for applications such as laser imaging, LiDAR (light detection and ranging)⁴⁸, laser displays⁴⁹, photon computing⁵⁰ and on-chip communications⁵¹. It is anticipated that, using other III–V gain media such as InP and GaAs, proportionally smaller devices could be realized at shorter wavelengths down to 800 nm. The substitution of gold with silver may lead to narrower linewidths. It should be possible to control the particle size and shape more precisely using advanced lithography with deep-ultraviolet or nanoparticle masks⁵². Our metal–semiconductor design has enabled us to produce plasmonic laser particles that emit narrowband light across a broad spectral range. Compared with previously demonstrated photonic laser particles in the same short-wavelength infrared region^{41,43}, the plasmonic laser particles are approximately 2.5 times smaller in lateral size and six times smaller in volume and weight. This reduction is significant and

advantageous in cellular applications, particularly for small, mobile immune cells (see Supplementary Fig. 4). The smaller size minimizes physical interference with cells and their migration⁴², facilitates the tagging of cells with multiple laser particles for tracking through cell division and may enable the tagging of subcellular organelles, such as nuclei. These cell-barcoding nanolasers hold promise for various applications, including large-scale multiplexed imaging, single-cell analysis and plasmonic sensing^{37,39–41}.

Online content

Any methods, additional references, Nature Portfolio reporting summaries, source data, extended data, supplementary information, acknowledgements, peer review information; details of author contributions and competing interests; and statements of data and code availability are available at <https://doi.org/10.1038/s41565-024-01843-7>.

References

- Kogelnik, H. & Shank, C. V. Coupled-wave theory of distributed feedback lasers. *J. Appl. Phys.* **43**, 2327–2335 (1972).
- Akahane, Y., Asano, T., Song, B.-S. & Noda, S. High-Q photonic nanocavity in a two-dimensional photonic crystal. *Nature* **425**, 944–947 (2003).
- Nozaki, K., Kita, S. & Baba, T. Room temperature continuous wave operation and controlled spontaneous emission in ultrasmall photonic crystal nanolaser. *Opt. Express* **15**, 7506–7514 (2007).
- Mao, X.-R., Shao, Z.-K., Luan, H.-Y., Wang, S.-L. & Ma, R.-M. Magic-angle lasers in nanostructured moiré superlattice. *Nat. Nanotechnol.* **16**, 1099–1105 (2021).
- Luan, H.-Y., Ouyang, Y.-H., Zhao, Z.-W., Mao, W.-Z. & Ma, R.-M. Reconfigurable moiré nanolaser arrays with phase synchronization. *Nature* **624**, 282–288 (2023).
- Hill, M. T. et al. Lasing in metallic-coated nanocavities. *Nat. Photon.* **1**, 589–594 (2007).
- Yu, Y., Lakhani, A. & Wu, M. C. Subwavelength metal-optic semiconductor nanopatch lasers. *Opt. Express* **18**, 8790–8799 (2010).
- Berini, P. & De Leon, I. Surface plasmon–polariton amplifiers and lasers. *Nat. Photon.* **6**, 16–24 (2012).

9. Oulton, R. F. et al. Plasmon lasers at deep subwavelength scale. *Nature* **461**, 629–632 (2009).
10. Maslov, A. V. & Ning, C.-Z. Size reduction of a semiconductor nanowire laser by using metal coating. In *Physics and Simulation of Optoelectronic Devices XV* Vol. 6468 (eds Osinski, M. et al.) 64680I (SPIE, 2007).
11. Azzam, S. I. et al. Ten years of spasers and plasmonic nanolasers. *Light Sci. Appl.* **9**, 90 (2020).
12. Ma, R.-M. & Oulton, R. F. Applications of nanolasers. *Nat. Nanotechnol.* **14**, 12–22 (2019).
13. Khajavikhan, M. et al. Thresholdless nanoscale coaxial lasers. *Nature* **482**, 204 (2012).
14. Lu, Y.-J. et al. Plasmonic nanolaser using epitaxially grown silver film. *Science* **337**, 450–453 (2012).
15. Wu, C.-Y. et al. Plasmonic green nanolaser based on a metal–oxide–semiconductor structure. *Nano Lett.* **11**, 4256–4260 (2011).
16. Ma, R.-M., Oulton, R. F., Sorger, V. J., Bartal, G. & Zhang, X. Room-temperature sub-diffraction-limited plasmon laser by total internal reflection. *Nat. Mater.* **10**, 110–113 (2011).
17. Sidiropoulos, T. P. H. et al. Ultrafast plasmonic nanowire lasers near the surface plasmon frequency. *Nat. Phys.* **10**, 870–876 (2014).
18. Kwon, S.-H. et al. Subwavelength plasmonic lasing from a semiconductor nanodisk with silver nanopan cavity. *Nano Lett.* **10**, 3679–3683 (2010).
19. Nezhad, M. P. et al. Room-temperature subwavelength metallo-dielectric lasers. *Nat. Photon.* **4**, 395–399 (2010).
20. Oulton, R. F., Sorger, V. J., Genov, D. A., Pile, D. F. P. & Zhang, X. A hybrid plasmonic waveguide for subwavelength confinement and long-range propagation. *Nat. Photon.* **2**, 496–500 (2008).
21. Huang, J., Kim, S.-H. & Scherer, A. Design of a surface-emitting, subwavelength metal-clad disk laser in the visible spectrum. *Opt. Express* **18**, 19581–19591 (2010).
22. Zhou, W. et al. Lasing action in strongly coupled plasmonic nanocavity arrays. *Nat. Nanotechnol.* **8**, 506–511 (2013).
23. Bergman, D. J. & Stockman, M. I. Surface plasmon amplification by stimulated emission of radiation: quantum generation of coherent surface plasmons in nanosystems. *Phys. Rev. Lett.* **90**, 027402 (2003).
24. Kewes, G. et al. Limitations of particle-based spasers. *Phys. Rev. Lett.* **118**, 237402 (2017).
25. Wang, Z., Meng, X., Kildishev, A. V., Boltasseva, A. & Shalaev, V. M. Nanolasers enabled by metallic nanoparticles: from spasers to random lasers. *Laser Photon. Rev.* **11**, 1700212 (2017).
26. Wu, H. et al. Plasmonic nanolasers: pursuing extreme lasing conditions on nanoscale. *Adv. Opt. Mater.* **7**, 1900334 (2019).
27. Lu, Y.-J. et al. All-color plasmonic nanolasers with ultralow thresholds: autotuning mechanism for single-mode lasing. *Nano Lett.* **14**, 4381–4388 (2014).
28. Wang, S. et al. Unusual scaling laws for plasmonic nanolasers beyond the diffraction limit. *Nat. Commun.* **8**, 1889 (2017).
29. Cho, S., Yang, Y., Soljačić, M. & Yun, S. H. Submicrometer perovskite plasmonic lasers at room temperature. *Sci. Adv.* **7**, eabf3362 (2021).
30. Noginov, M. A. et al. Demonstration of a spaser-based nanolaser. *Nature* **460**, 1110–1112 (2009).
31. Park, Y.-S., Roh, J., Diroll, B. T., Schaller, R. D. & Klimov, V. I. Colloidal quantum dot lasers. *Nat. Rev. Mater.* **6**, 382–401 (2021).
32. Galanzha, E. I. et al. Spaser as a biological probe. *Nat. Commun.* **8**, 15528 (2017).
33. Peña, O. & Pal, U. Scattering of electromagnetic radiation by a multilayered sphere. *Comput. Phys. Commun.* **180**, 2348–2354 (2009).
34. Feigenbaum, E. & Orenstein, M. Ultrasmall volume plasmons, yet with complete retardation effects. *Phys. Rev. Lett.* **101**, 163902 (2008).
35. Meier, M. & Wokaun, A. Enhanced fields on large metal particles: dynamic depolarization. *Opt. Lett.* **8**, 581–583 (1983).
36. Wang, F. & Shen, Y. R. General properties of local plasmons in metal nanostructures. *Phys. Rev. Lett.* **97**, 206806 (2006).
37. Rybin, M. V. et al. High-Q supercavity modes in subwavelength dielectric resonators. *Phys. Rev. Lett.* **119**, 243901 (2017).
38. Olsen, G. & Zamerowski, T. Vapor-phase growth of (In,Ga)(As,P) quaternary alloys. *IEEE J. Quantum Electron.* **17**, 128–138 (1981).
39. Sarkar, D. et al. Ultrasmall InGa(As)P dielectric and plasmonic nanolasers. *ACS Nano* **17**, 16048–16055 (2023).
40. Bernstein, L. et al. Ultrahigh resolution spectral-domain optical coherence tomography using the 1000–1600 nm spectral band. *Biomed. Opt. Express* **13**, 1939–1947 (2022).
41. Martino, N. et al. Wavelength-encoded laser particles for massively-multiplexed cell tagging. *Nat. Photon.* **13**, 720–727 (2019).
42. Fikouras, A. H. et al. Non-obstructive intracellular nanolasers. *Nat. Commun.* **9**, 4817 (2018).
43. Kwok, S. J. J. et al. High-dimensional multi-pass flow cytometry via spectrally encoded cellular barcoding. *Nat. Biomed. Eng.* **8**, 310–324 (2024).
44. Cho, S., Humar, M., Martino, N. & Yun, S. H. Laser particle stimulated emission microscopy. *Phys. Rev. Lett.* **117**, 193902 (2016).
45. Schubert, M. et al. Monitoring contractility in cardiac tissue with cellular resolution using biointegrated microlasers. *Nat. Photon.* **14**, 452–458 (2020).
46. Maniyara, R. A. et al. Tunable plasmons in ultrathin metal films. *Nat. Photon.* **13**, 328–333 (2019).
47. Yun, S. H. & Kwok, S. J. J. Light in diagnosis, therapy and surgery. *Nat. Biomed. Eng.* **1**, 0008 (2017).
48. Li, B., Lin, Q. & Li, M. Frequency–angular resolving LiDAR using chip-scale acousto-optic beam steering. *Nature* **620**, 316–322 (2023).
49. Zhao, J. et al. Full-color laser displays based on organic printed microlaser arrays. *Nat. Commun.* **10**, 870 (2019).
50. Chen, Z. et al. Deep learning with coherent VCSEL neural networks. *Nat. Photon.* **17**, 723–730 (2023).
51. Wang, Y., Holguín-Lerma, J. A., Vezzoli, M., Guo, Y. & Tang, H. X. Photonic-circuit-integrated titanium: sapphire laser. *Nat. Photon.* **17**, 338–345 (2023).
52. Totzeck, M., Ulrich, W., Göhnermeier, A. & Kaiser, W. Pushing deep ultraviolet lithography to its limits. *Nat. Photon.* **1**, 629–631 (2007).

Publisher's note Springer Nature remains neutral with regard to jurisdictional claims in published maps and institutional affiliations.

Springer Nature or its licensor (e.g. a society or other partner) holds exclusive rights to this article under a publishing agreement with the author(s) or other rightsholder(s); author self-archiving of the accepted manuscript version of this article is solely governed by the terms of such publishing agreement and applicable law.

© The Author(s), under exclusive licence to Springer Nature Limited 2025

Methods

Materials

Custom semiconductor wafers comprising epitaxial layers via metal-organic chemical vapour deposition on InP substrates were ordered from Seen Semiconductors. Gold substrates, purchased from Platypus, had a measured surface roughness of 1.2 nm. H₂SO₄ was purchased from Transene Company. All other chemicals, such as H₂O₂, HCl, tetraethyl orthosilicate, polyethyleneimine and ammonium hydroxide, were purchased from Sigma-Aldrich.

Half-wave device fabrication

We used an epitaxial wafer with three layers of undoped InGaAsP with different stoichiometries, separated by InP sacrificial layers. Mesa structures were fabricated using optical lithography and reactive-ion etching to a diameter of 0.9–1.0 μm. Among the three InGaAsP materials (In_{0.53}Ga_{0.47}As_{0.92}P_{0.08}, In_{0.53}Al_{0.13}Ga_{0.34}As and In_{0.8}Ga_{0.2}As_{0.44}P_{0.56}), we used In_{0.53}Ga_{0.47}As_{0.92}P_{0.08} or In_{0.8}Ga_{0.2}As_{0.44}P_{0.56} layers, with an initial thickness of 290 or 200 nm, respectively. The diameter of the InGaAsP layer was adjusted by immersing the wafer chip in acid piranha solution (H₂SO₄:H₂O₂:H₂O = 1:1:10) and etching for a pre-calibrated reaction time³⁹. Next, the InP layers were removed using HCl, which released the InGaAsP particles⁴¹. The particles were washed with ethanol and water, then dispersed in ethanol. The InGaAsP particles were further etched in piranha solution (same composition) to achieve the final desired thickness and lateral size, based on pre-calibrated reaction times. Submicrometre particles typically acquired rhombus shapes due to anisotropic etching rates across the different lattice planes of InGaAsP. For SiO₂ coating, we used the Stöber method⁴¹. The SiO₂-coated particles were washed multiple times with ethanol and water before being drop-cast on to designated gold- or SiO₂-coated silicon substrates.

Optical measurements

We used a commercial laser-scanning microscope (Olympus, FVMPE-RS) for optical characterization. The laser-scanning unit of the microscope was coupled with both nanosecond and picosecond pump lasers. The nanosecond pump laser (IPG Photonics, YLPN-1-1×120-50-M) at 1,064 nm had a tunable pulse duration ranging from 1 to 120 ns and a variable repetition rate from 2 kHz to 14 MHz. For shorter pump pulses, we used a picosecond pump laser (Picoquant, VisIR-765) with a pulse duration of 70 ps, a centre wavelength of 765 nm and a repetition rate that was variable from 2.5 to 80 MHz. An NIR-optimized, ×100, 0.85 NA (numerical aperture) objective (Olympus IMS LCPLN100xIR) was used for optical pumping. The output emission from the samples was collected through the same lens and directed to an NIR spectrometer via a dichroic mirror. An InGaAs linescan camera (Sensor Unlimited 2048L) was used for spectral characterization with a typical integration time of 1 ms. The spectrometer had a diffraction grating with 200 lines per millimetre, providing a resolution of 0.8 nm and a wavelength span of 1,100–1,600 nm. For low-temperature experiments, we placed the samples on a thermoelectric cooler connected to a chiller. For time-resolved photoluminescence measurements, we used the picosecond laser (VisIR-765) with a repetition rate of 40 MHz, a single-photon InGaAs avalanche photodiode (Micro Photonics Devices) with a timing jitter of 100 ps and a time-correlated single-photon counting board (TimeHarp 260, PicoQuant) with a resolution of 25 ps. For the far-field emission and speckle imaging, we used a silicon-based EMCCD camera (Luca, Andor) in a wide-field configuration, along with a spectrometer (Shamrock, Andor) equipped with a silicon-based EMCCD (Newton, Andor) and a diffraction grating (300 lines per millimetre; 500 nm blaze) for a resolution of 0.67 nm. The pump source was the picosecond laser (VisIR-765) at 765 nm with a 2.5 MHz repetition rate. A long-pass dichroic filter with an 850 nm cut-off were used for sample excitation and emission detection. The pump beam was expanded using a 4f telescope to a full-width at half-maximum of approximately 15 μm in the focal plane. 3M Scotch Magic tape was applied to the sample on a

gold substrate as a scattering medium. Pump excitation and detection were conducted in an epi-fluorescence configuration.

Numerical simulations

FDTD calculations of the Mie scattering spectra and dipole-embedded cavity mode properties were performed using commercial software (Lumerical FDTD Solutions). More details are available in Supplementary Note 5.

Semiconductor laser modelling

The rate equations of a semiconductor laser were formulated and solved numerically using MATLAB in a laptop. Briefly, for electron-hole pairs (q) the energy states are divided into typically 120 levels (that is, $k = 1-120$) and the numbers of emitters (n_k) within individual levels centred at ω_k evolve over time (t) via pumping (P_k), stimulated emission ($q \times \tau_s^{-1}$), spontaneous emission (τ_s^{-1}) and non-radiative decay to lower levels (τ_{nr}^{-1}). The photon numbers (q_k) with energies labelled from 1 to 120 are varied over time through stimulated emission, spontaneous emission and cavity loss (τ_c^{-1}). Thermodynamic excitation was neglected for computational simplicity.

For numbers of electron-hole pairs in the first (band edge) to the k th (pump) levels:

$$\frac{dn_k}{dt} = P_k(t) - \frac{n_k}{\tau_s(\omega_k)} - \frac{n_k}{\tau_{nr}(\omega_k)} \quad (2)$$

$$\frac{dn_{k-1}}{dt} = -\frac{\Delta\Omega}{\delta\omega} \frac{n_{k-1}q_{k-1}}{\tau_s(\omega_{k-1})} - \frac{n_{k-1}}{\tau_s(\omega_{k-1})} - \frac{n_{k-1}}{\tau_{nr}(\omega_{k-1})} \quad (3)$$

$$\frac{dn_{k-2}}{dt} = -\frac{\Delta\Omega}{\delta\omega} \frac{n_{k-2}q_{k-2}}{\tau_s(\omega_{k-2})} - \frac{n_{k-2}}{\tau_s(\omega_{k-2})} - \frac{n_{k-2}}{\tau_{nr}(\omega_{k-2})} \dots \quad (4)$$

$$\frac{dn_1}{dt} = -\frac{\Delta\Omega}{\delta\omega} \frac{n_1q_1}{\tau_s(\omega_1)} - \frac{n_1}{\tau_s(\omega_1)} \quad (5)$$

For photons (polaritons) in the i th level (i ranging from 1 to $k-1$):

$$\frac{dq_i}{dt} = \frac{\Delta\Omega}{\delta\omega} \frac{n_iq_i}{\tau_s(\omega_i)} + \frac{n_i}{\tau_s(\omega_i)} - \frac{q_i}{\tau_c(\omega_i)} \quad (6)$$

The transition rate coefficients depend on the resonance centre frequency ω_0 and the bandwidth $\Delta\Omega$ with constants including the cavity lifetime at the resonance frequency τ_{c0} , non-radiative decay time constant τ_{nr0} and maximum carrier density at saturation n_{sat} :

$$\frac{1}{\tau_s(\omega_i)} = \frac{1}{\tau_s} \cdot \frac{\Delta\Omega^2/4}{(\omega_i - \omega_0)^2 + \Delta\Omega^2/4} \quad (7)$$

$$\frac{1}{\tau_c(\omega_i)} = \frac{1}{\tau_{c0}} \cdot \frac{\Delta\Omega^2/4}{(\omega_i - \omega_0)^2 + \Delta\Omega^2/4} \quad (8)$$

$$\frac{1}{\tau_{nr}(\omega_i)} = \frac{1}{\tau_{nr0}} \cdot \frac{n_{sat}(\omega_{i-1}) - n_{i-1}}{n_0} \quad (9)$$

Details are described in Supplementary Note 3.

Fabrication of metal-coated semiconductor particles

To produce stand-alone laser particles, we used an In_{0.73}Ga_{0.27}As_{0.58}P_{0.42} single-layer wafer. After optical lithography and reactive-ion etching, pillars with a diameter of 2 μm were created⁴¹. The diameter of the InGaAsP layer was reduced by immersing the wafer chip in acid piranha solution (H₂SO₄:H₂O₂:H₂O = 1:1:10) for a specific etching duration³⁹. Subsequently, HCl or H₃PO₄ was used to etch InP sacrificial layers to diameters that

roughly matched that of the InGaAsP layer as well as removing an InP cap layer on top of the InGaAsP layer. After washing the wafer, a 5-nm-thick SiO₂ coating was produced on the pillars using the Stöber method⁴¹. A layer of gold was deposited on the pillar array using an electron-beam evaporator (Denton EE-4, Harvard Center for Nanoscale Systems). By immersing the wafer in HCl, the gold-deposited metal–semiconductor particles were detached from the substrate. The harvested particles were washed three times with fresh water and ethanol. To enhance the material stability and biocompatibility in aqueous media and cytoplasm, an approximately 60-nm-thick SiO₂ shell was added to the particles via the Stöber method over three cycles⁴¹. To further enhance the biocompatibility and facilitate cellular uptake, the SiO₂-coated metal–semiconductor particles were encapsulated with polyethyleneimine polymer.

Cell experiments

Green-fluorescent-protein-expressing HeLa human cervical cancer cells were purchased from GenTarget. The HeLa cells were cultured in Dulbecco's modified Eagle medium, supplemented with 10% (v/v) fetal bovine serum and 1% (v/v) penicillin–streptomycin, at 37 °C under 5% CO₂. For cell tagging, cells at the desired density were plated on a glass-bottomed plate with the cell medium. Metal–semiconductor laser particles suspended in the same cell culture medium were added to the cell-containing plate. The plate was shaken to evenly disperse the laser particles. After 24 h of incubation, cell laser experiments were performed using a customized microscope.

Reporting summary

Further information on research design is available in the Nature Portfolio Reporting Summary linked to this article.

Data availability

The laser experiment data used within this paper are available via the Harvard Dataverse at <https://doi.org/10.7910/DVN/AOWZN8>. Additional data that support the findings of this study are available from the corresponding author upon reasonable request.

Code availability

The code used for the semiconductor laser modelling and analysis of the laser experiment data is available via Code Ocean and the Harvard Dataverse at <https://doi.org/10.7910/DVN/AOWZN8>. The code associated with the FDTD calculations is available from the corresponding author upon reasonable request.

Acknowledgements

K. Kim, Y. Wu and D. Sarkar are acknowledged for helpful discussions. This study was supported by National Institutes of Health research grants (R01-EB033155 and R01-EB034687). S.C. acknowledges the MGH Fund for Medical Discovery fundamental research fellowship award. This research used the resources of the Center for Nanoscale Systems, part of Harvard University, a member of the National Nanotechnology Coordinated Infrastructure, supported by the National Science Foundation under award number 1541959.

Author contributions

S.C. and S.-H.Y. designed the study. S.C. performed the experiments and FDTD simulations. N.M. contributed to the optical set-ups. S.-H.Y. conducted the semiconductor laser modelling. S.C. and S.-H.Y. analysed the data and wrote the paper.

Competing interests

N.M. and S.-H.Y. have financial interests in LASE Innovation Inc., a company focused on commercializing technologies that are based on laser particles. The financial interests of N.M. and S.-H.Y. were reviewed and are managed by Mass General Brigham in accordance with their conflict-of-interest policies. S.C. declares no competing interests.

Additional information

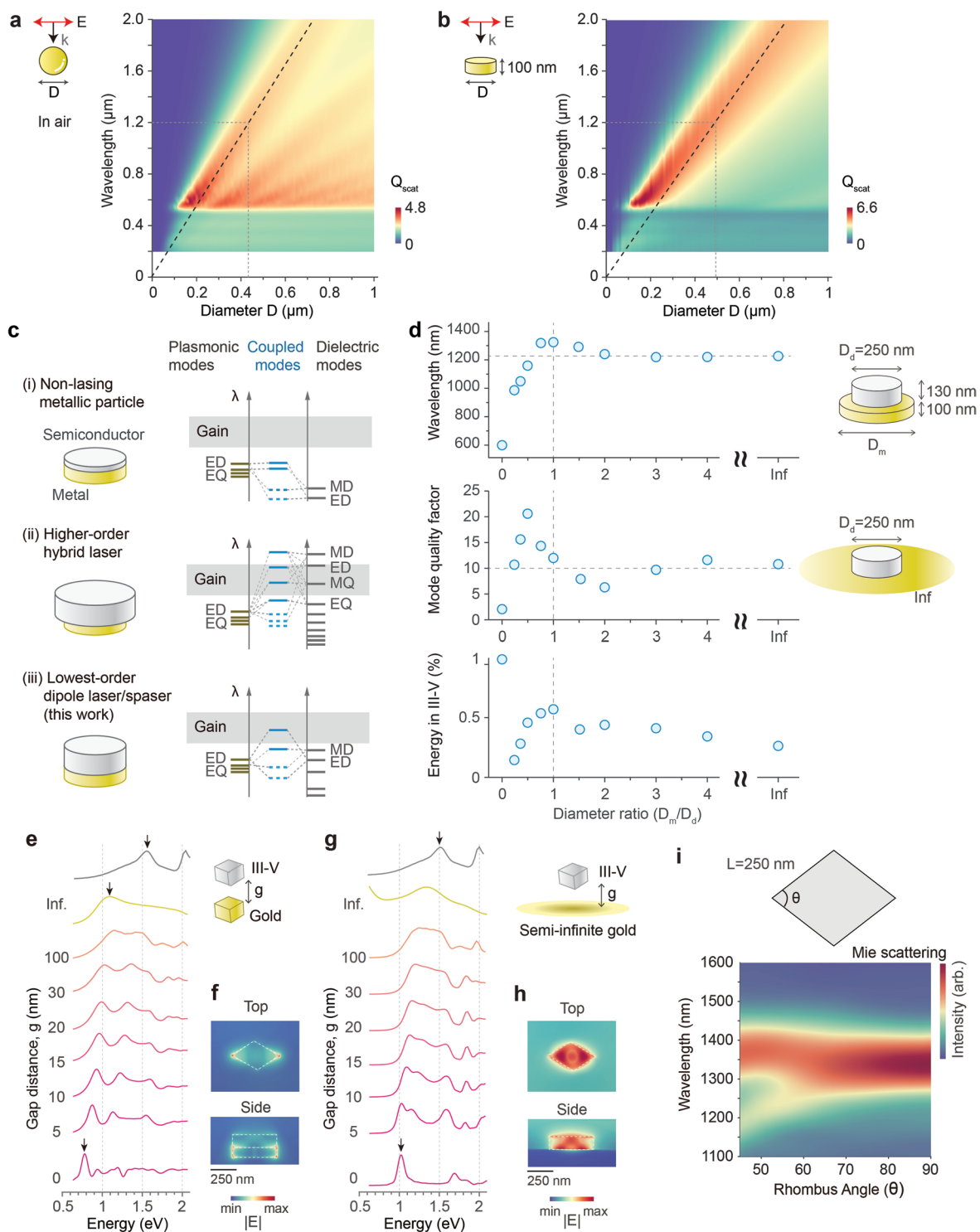
Extended data is available for this paper at <https://doi.org/10.1038/s41565-024-01843-7>.

Supplementary information The online version contains supplementary material available at <https://doi.org/10.1038/s41565-024-01843-7>.

Correspondence and requests for materials should be addressed to Seok-Hyun Yun.

Peer review information *Nature Nanotechnology* thanks the anonymous reviewers for their contribution to the peer review of this work.

Reprints and permissions information is available at www.nature.com/reprints.

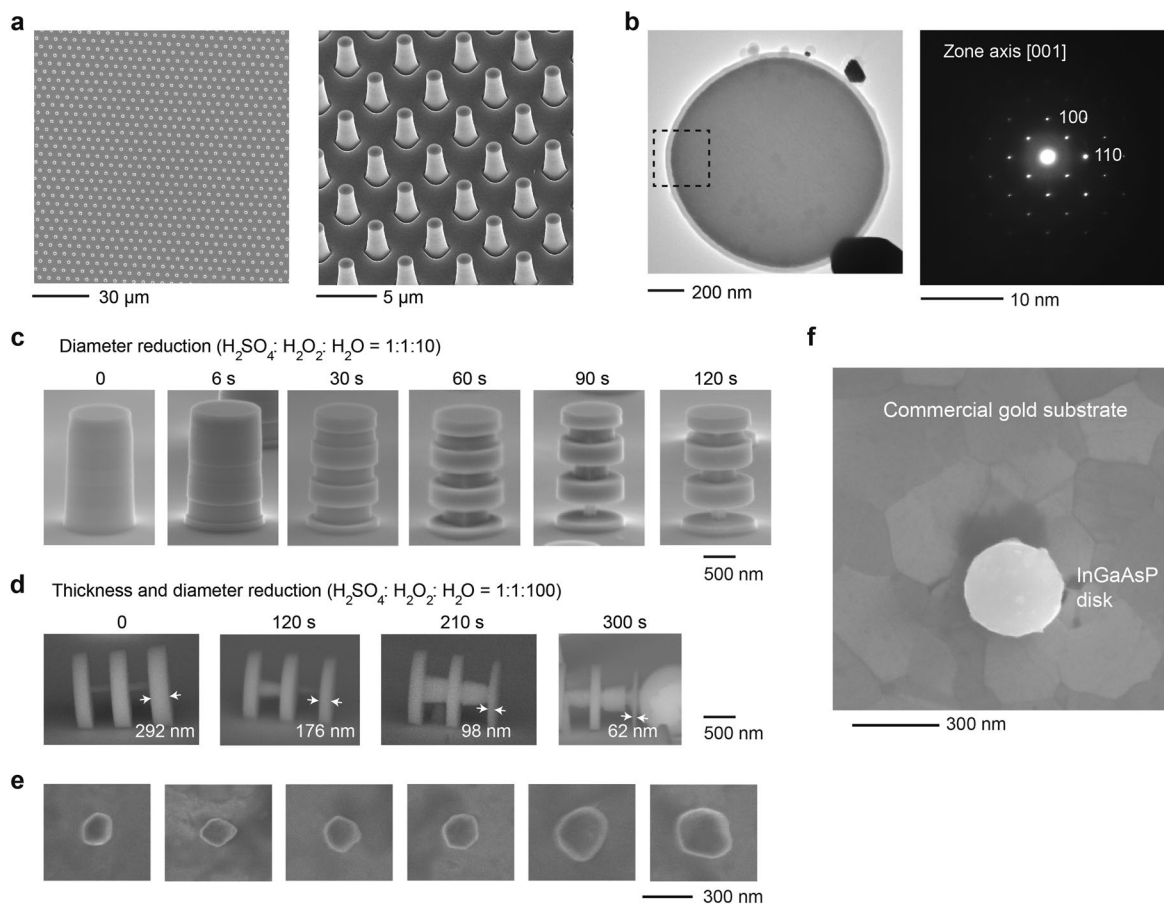


Extended Data Fig. 1 | See next page for caption.

Extended Data Fig. 1 | Mode properties of metal-semiconductor

nanoparticles. a–b, Mie scattering spectra of gold nano-spheres (a) and gold nano-discs (b) in air for planar incident waves. While the excitation of higher order modes is evident for spheres, only the fundamental electrical dipole mode clearly appears for discs owing to the symmetry; the higher modes in discs are not efficiently excited by the uniform driving field. In nano-lasers, however, higher-order plasmonic modes are driven by local emitters and can be efficiently excited via near-field interactions. **c**, Schematic depicting mode coupling between plasmonic and semiconductor disc modes for three representative cases: (i) Non-lasing metallic luminescence when a semiconductor disc is too thin. Because of the large differences of the modes in energy, mode coupling is weak, and the lowest order modes are largely plasmonic. Because of the mode proximity, it is difficult to selectively amplify only the ED mode; (ii) Higher-order hybrid laser, where multiple dielectric-like modes are present within a gain bandwidth; (iii) A hybrid dipole laser – which may be regarded a ‘spaser’ – where the individual modes in the metal and semiconductor discs have similar energies. Strong coupling occurs between ED modes, separating the hybrid plasmon-like mode from the other hybrid modes. This mode shift may be considered as the effect of the refractive index of the semiconductor on the plasmonic mode. However, mode coupling is a more accurate explanation as the effective index experienced by the plasmonic ED mode matches the index of the ED mode in the dielectric medium. Note that the MD modes, the lowest order modes in

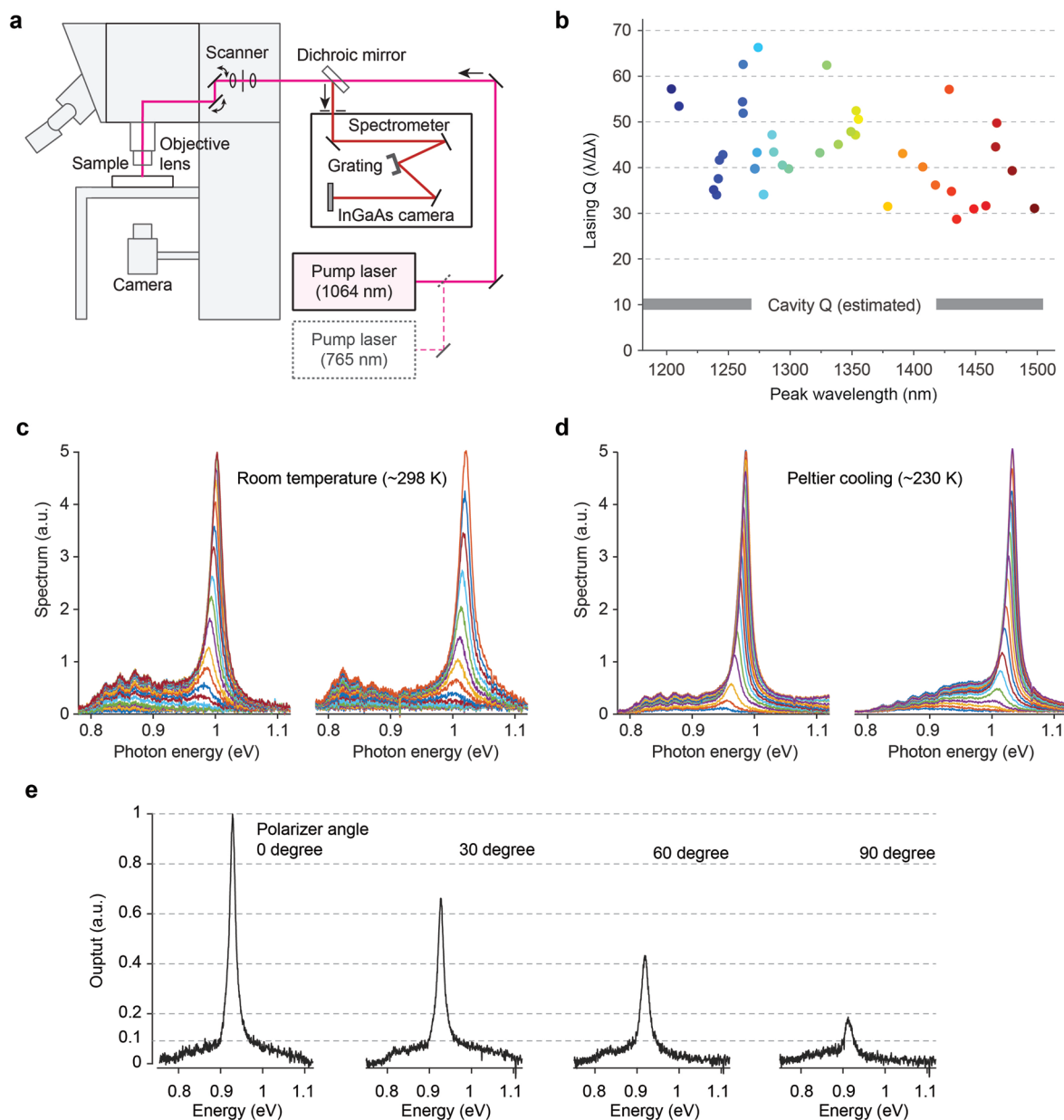
dielectric discs, are not efficiently coupled with the plasmonic ED mode because of the field symmetry. **d**, FDTD simulation of metal-semiconductor discs with different diameters, as depicted in the inset. The resonance wavelength, quality factor, and mode confinement factor in the semiconductor vary as a function of the diameter ratio from 0 (III-V only) to infinity (on a gold substrate). The resonance wavelength of the hybrid ED mode increases dramatically from 600 nm to 1300 nm at size matching and then 1220 nm for oversized gold. The quality factor reaches its maximum at a diameter ratio of 0.5, partly due to optimal mode energy matching and partly due to reduced metallic absorption at 800–900 nm. The Q factor approaches slightly over 10 at infinite gold, with a quarter of electromagnetic energy residing in the semiconductor while the remaining three quarters are stored in the metal. See Supplementary Fig. 2 for more examples of Mie scattering spectra. **e**, Simulated Mie scattering spectra of a complex of semiconductor ($n = 3.5$) and gold rhombus-like particles, each with a side length of 250 nm and heights of 130 nm and 100 nm, respectively, for various gap distances. The arrow indicates the lowest-order mode at contact. **f**, Electric field amplitude profiles of the semiconductor-gold particles in contact (dashed outline). **g**, Simulated Mie scattering spectra of a semiconductor on infinite substrates for different gap distances. The arrow indicates the lowest mode at contact. **h**, Electric field amplitude profiles of the semiconductor-on-gold structure. **i**, Simulated Mie scattering spectra of a rhombus-shaped semiconductor on an infinite substrate for different rhombus interior angles.



Extended Data Fig. 2 | Size and thickness tuning of semiconductor particles.

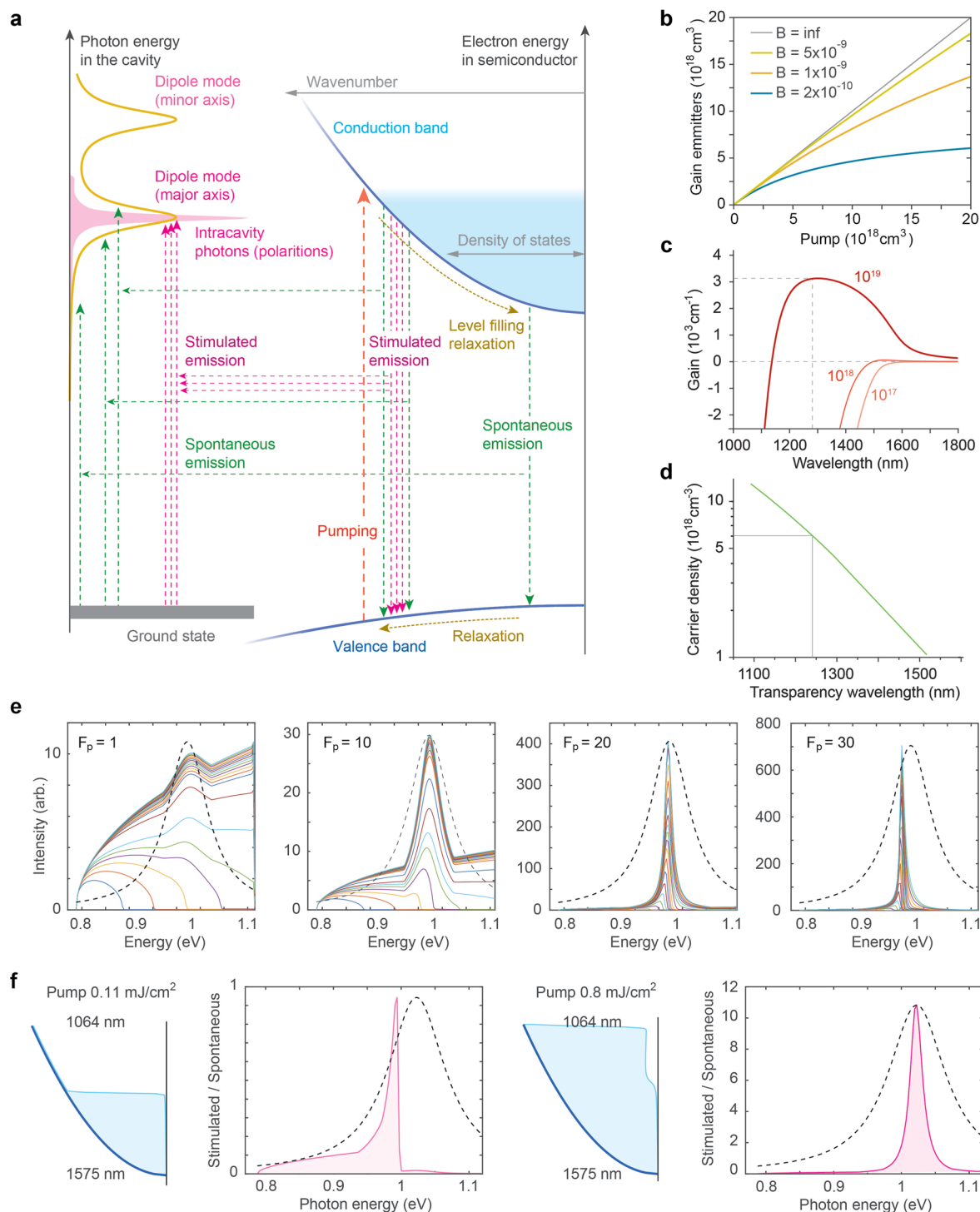
a, SEM images of a semiconductor wafer after RIE, showing pillars with a diameter of $1.21 \mu\text{m} \pm 45 \text{ nm}$. **b**, (Left) A high-resolution transmission electron micrograph (HRTEM) of a silica-coated microdisc; (Right) an electron diffraction (SAED) pattern from a selected area (dashed square). The zone axis is labeled as 001, and two lattice plane directions, 100 and 110, are marked for clarity. **c**, Two-dimensional etching for reducing the diameters of InGaAsP layers while preserving their thickness using piranha acid solution. The InP layer remains the same size while InGaAsP is etched away. The bottom layer with a composition of $\text{In}_{0.53}\text{Ga}_{0.47}\text{As}_{0.92}\text{P}_{0.08}$ was primarily used in most experiments (unless specified). **d**, Three-dimensional etching of InGaAsP layers, performed after a full (typically

or partial (for this dataset) etching of InP layers between InGaAsP layers. This process reduces both the thickness and lateral sizes. The 2D and 3D etching techniques were judiciously used to obtain desired thicknesses and sizes for InGaAsP particles. **e**, SEM images of six particles obtained from a single batch targeting a thickness of 130 nm and a mean side length of 250 nm. This batch was used to produce the experimental data in Fig. 2c. The variation in size and shape was largely introduced during the size reduction process via wet etching. More uniform discs could be produced from reduced pillar diameters. **f**, SEM image of an isolated semiconductor nanodisc placed on top of a gold-coated substrate. The polycrystalline domains of the gold layer are visualized.



Extended Data Fig. 3 | Half-wave dipolar lasers. **a**, Schematic of a microscope setup used for optical characterizations. **b**, Measured lasing linewidth Q factors of 40 devices with different sizes and shapes. Representative spectra are displayed in Fig. 2c. **c**, Emission spectra of two devices at a room temperature of 298 K. **d**, Emission spectra of two devices at a Peltier cooled temperature of -230 K (nominal). Compared to the room temperature spectra, the falling edges at the high energy side, or near the quasi-Fermi levels, are steeper, presumably

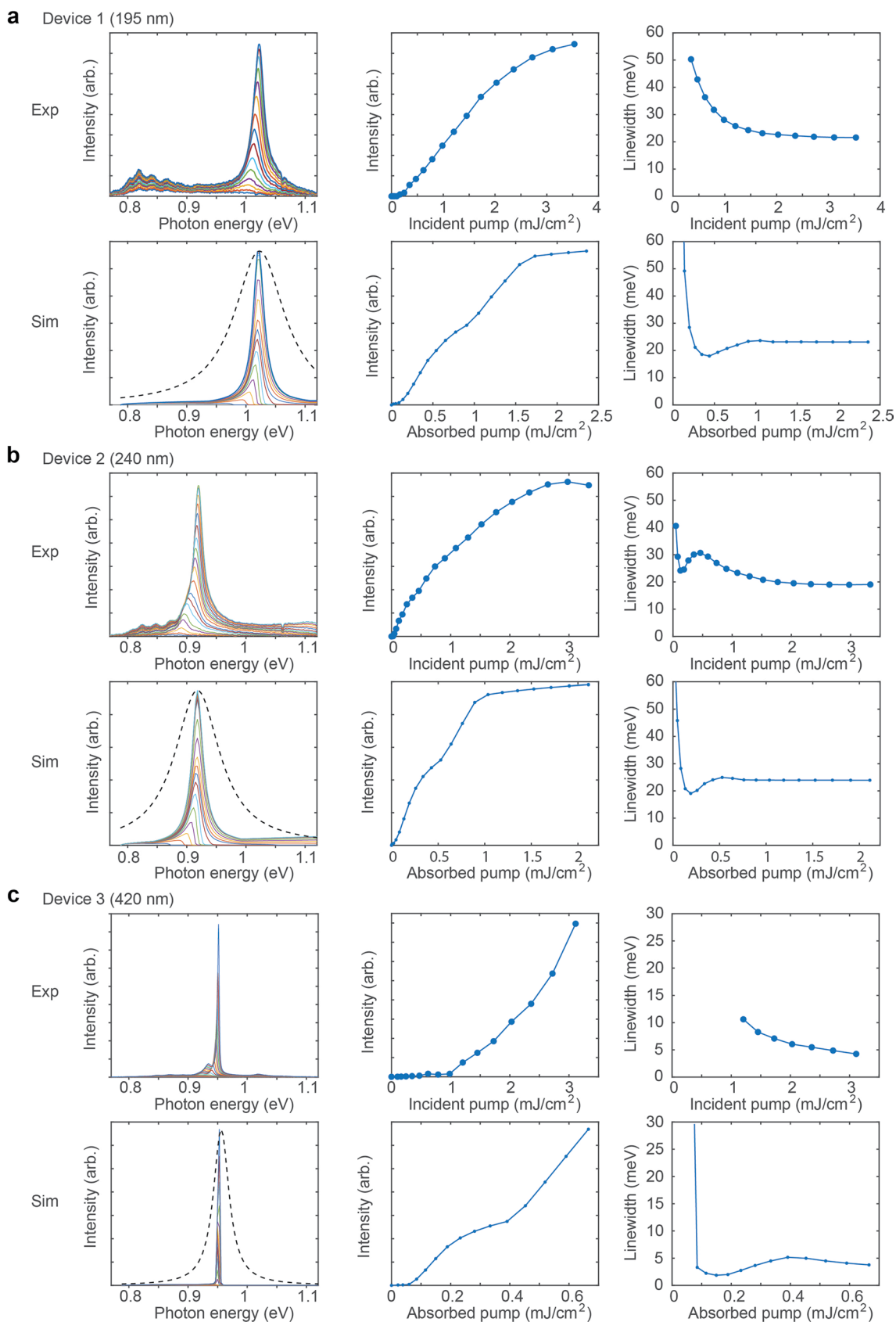
due to slightly reduced thermal excitations at the lower temperature. Note that the simulated spectra exhibit ever steeper spectral falloff at the quasi-Fermi level (see Fig. 3b and Extended Data Fig. 6), because no thermal excitations have been considered in the model, which corresponds to zero-degree temperature (0 K). **e**, Output spectra through a polarizer at different angles. The stimulated emission peak at 0.94 eV (1321 nm) is linear polarized while the broad lower-energy background above the peak (0.75 to 0.9 eV) is approximately unpolarized.



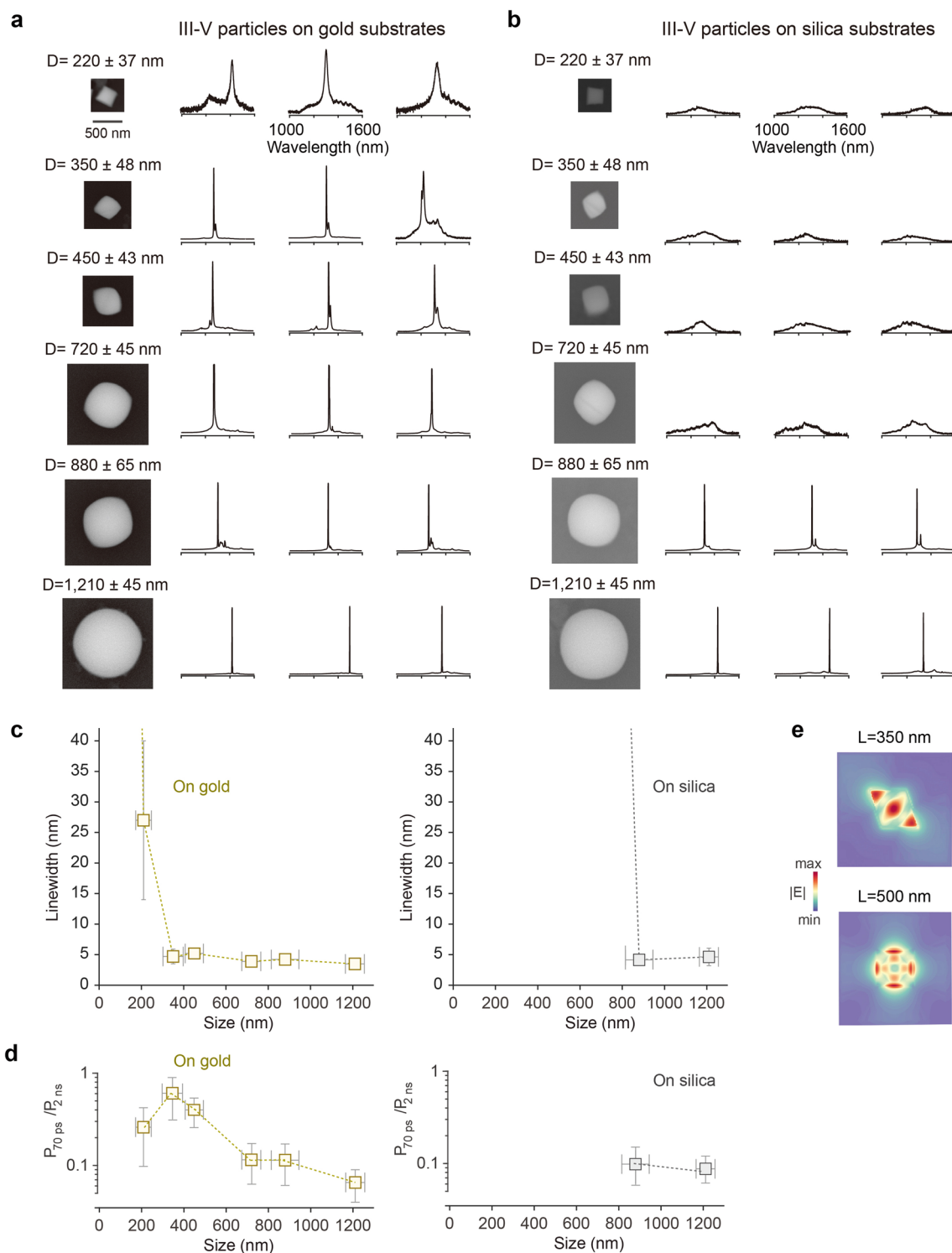
Extended Data Fig. 4 | Semiconductor gain and a 'waterfall' laser model.

a, Energy level diagram and various transitions paths in a semiconductor laser. This essentially forms a four-level laser system (or a quasi-three-level including valence band absorption of intracavity light). The blue shade represents free electrons (or the electron-hole plasma) that fill the electronic states in the conduction band. The simplified 'waterfall' model depicted in Fig. 3a is based on this diagram. **b**, Analysis of charge carrier loss due to Auger recombination for bulk (blue) and Purcell-enhanced (yellow) radiative decays. See Supplementary Note 2. **c**, Gain profiles at room temperature at three different carrier density levels, calculated using standard semiconductor theory considering the Fermi-Dirac distribution of the carriers at room temperature. Thermodynamic excitation was neglected in our numerical modeling, resulting a sharp gain cliff beyond the quasi-Fermi level. **d**, Calculated total carrier density versus

transparency (zero-gain) wavelength. **e**, Simulated output spectra of a device with a size of 240 nm for the cases of different Purcell factors, from 1 to 30, as the pump fluence is varied from 0.021 to 2.1 mJ/cm². The output saturates. The dashed curve illustrates the cold-cavity mode profile with a Q factor of 10. At $F_p = 1$, the lasing threshold is never reached even at extreme pumping levels. At $F_p = 10$, the lasing threshold is barely reached with a stimulated-to-spontaneous ratio of 1.07. Compared to $F_p = 20$, $F_p = 30$ results in reduced linewidths. Best correspondence to experimental data was obtained with $F_p = 18$ (Device 1) and $F_p = 19$ (Device 2). **f**, (Left) The emitter population and stimulated-to-spontaneous ratio at a threshold pump fluence, where the quasi-Fermi level is just below the modal resonant frequency. (Right) At a pump level 7.3 times above the threshold when all the entire excited states are almost filled.

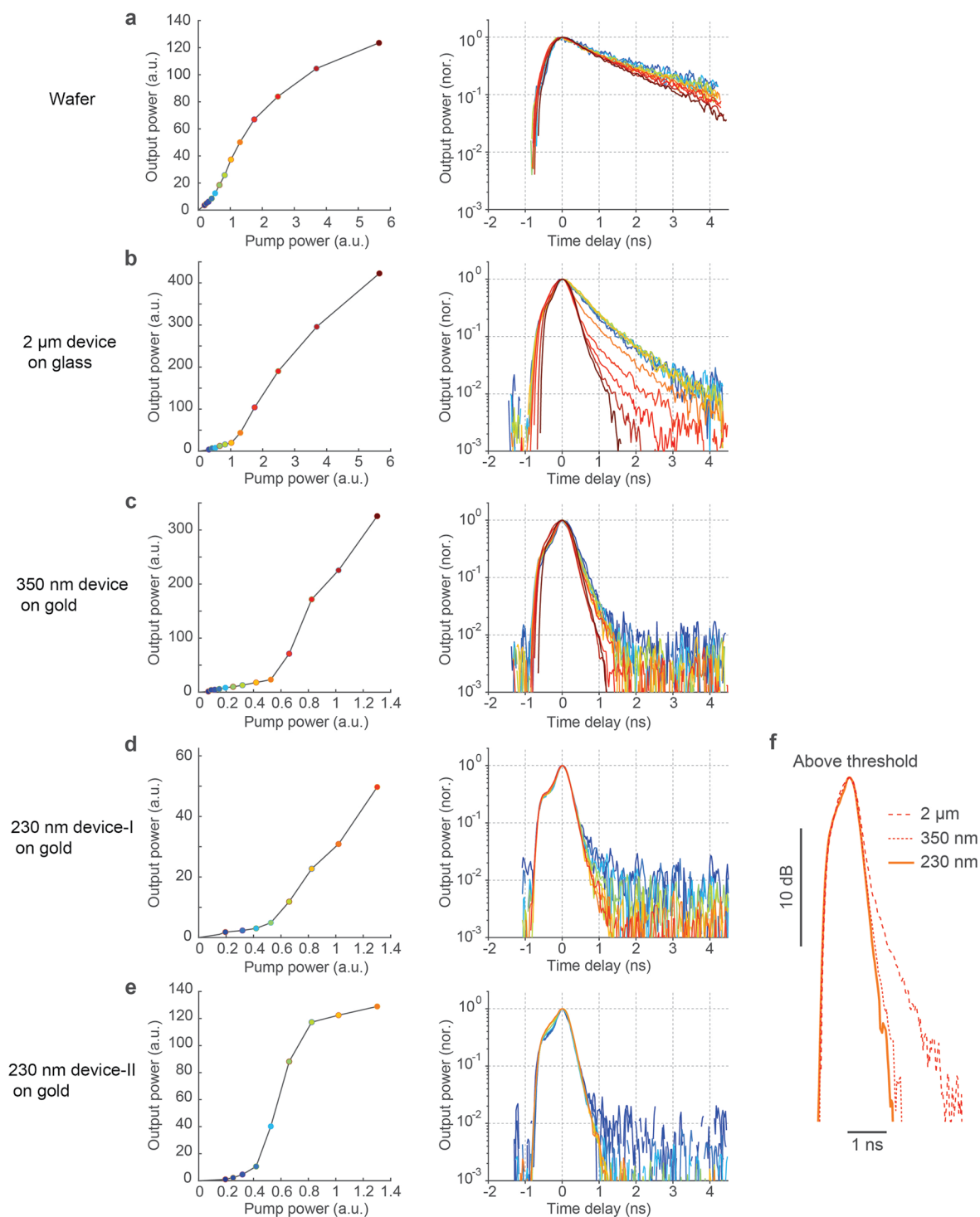


Extended Data Fig. 5 | Laser simulation and experimental results. a, Half-wave device (semiconductor volume: $183 \times 183 \times 130 \text{ nm}^3$). **b**, Half-wave device ($225 \times 225 \times 130 \text{ nm}^3$). **c**, One-wave device ($400 \times 400 \times 130 \text{ nm}^3$).



Extended Data Fig. 6 | Higher-order mode devices. **a–b**, Representative devices from different batches of varying sizes (same thickness of 290 nm) for plasmonic **(a)** and dielectric cavities **(b)**. Dielectric devices with less than 880 nm sizes did not reach lasing threshold even at the highest pump power levels. **c**, Emission linewidths measured from six different size batches, with a total of 120 devices and 15 samples per batch. The threshold pump fluences of these devices are shown in Fig. 2. The box in the error bar represents the mean

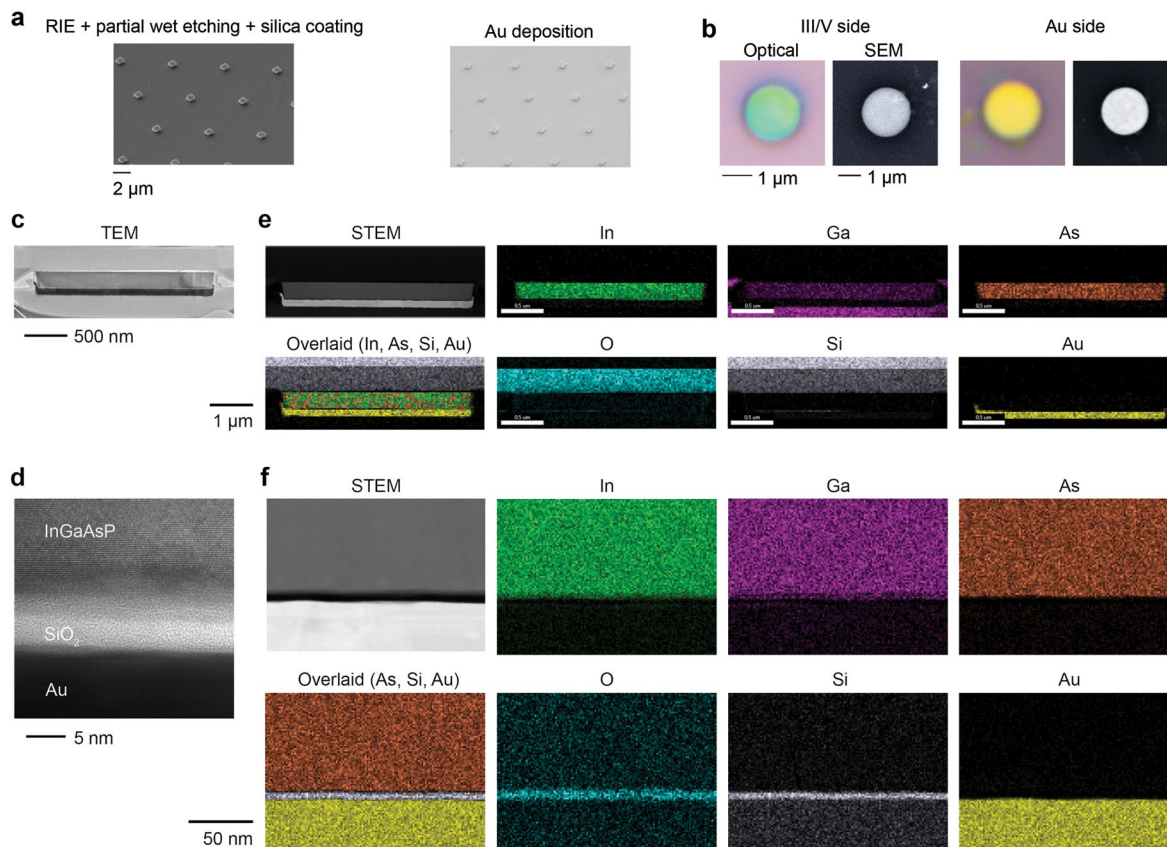
value, while the whiskers show the standard deviation. **d**, The ratio between the peak threshold powers for picosecond and nanosecond pumping of the devices batches, as shown in Fig. 2 and Extended Data Fig. 6c. Again, the box in the error bar represents the mean value, while the whiskers show the standard deviation. **e**, FDTD results of a 350-nm rhombus-shape showing a second order mode at 1206 nm (top) and a rectangular-shape 500-nm device showing a whispering gallery mode ($Q = 94$) at 1164 nm (bottom).



Extended Data Fig. 7 | Temporal responses of picosecond-pumped devices.

a-e, Output intensity (left) and temporal (right) curves at varying pump powers from four representative devices: **a**, a pristine semiconductor wafer; **b**, a photonic microlaser with a diameter of approximately 2 μm placed on a glass substrate; **c**, a plasmonic nanodisc device with a diameter of approximately 350 nm on a gold substrate; and **d-e**, two different nanodisc devices with a diameter of approximately 230 nm on a gold substrate. Colors represent

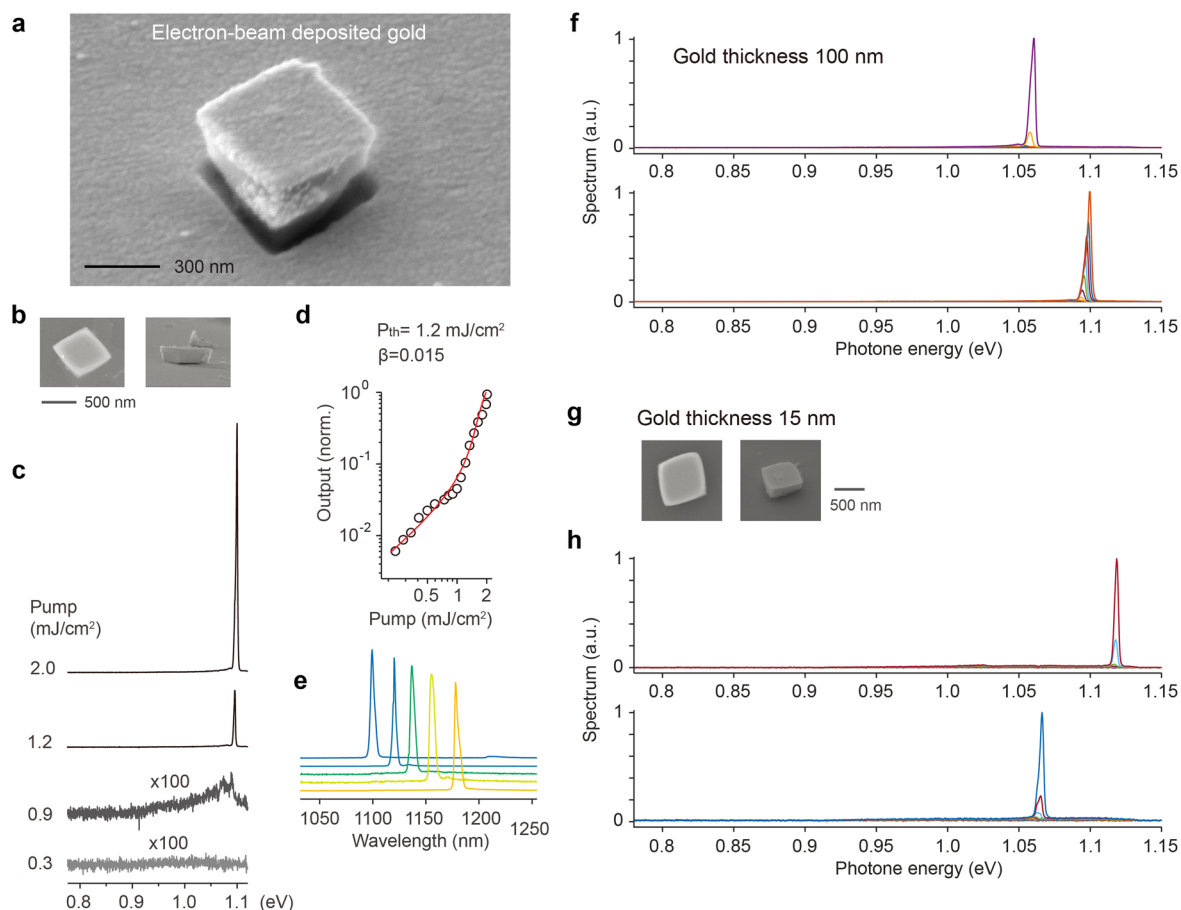
measurements at different pump powers. All laser devices exhibit kink behaviors indicative of the lasing threshold and accelerated lifetime. **f**, Superimposition of three representative temporal curves obtained from the devices in **a**, **b**, and **d**, above their respective lasing thresholds. The temporal profiles in the vicinity of the peak are nearly identical, indicating they are limited by the finite temporal resolution of the measurement instrument.



Extended Data Fig. 8 | Structure of metal-semiconductor particles.

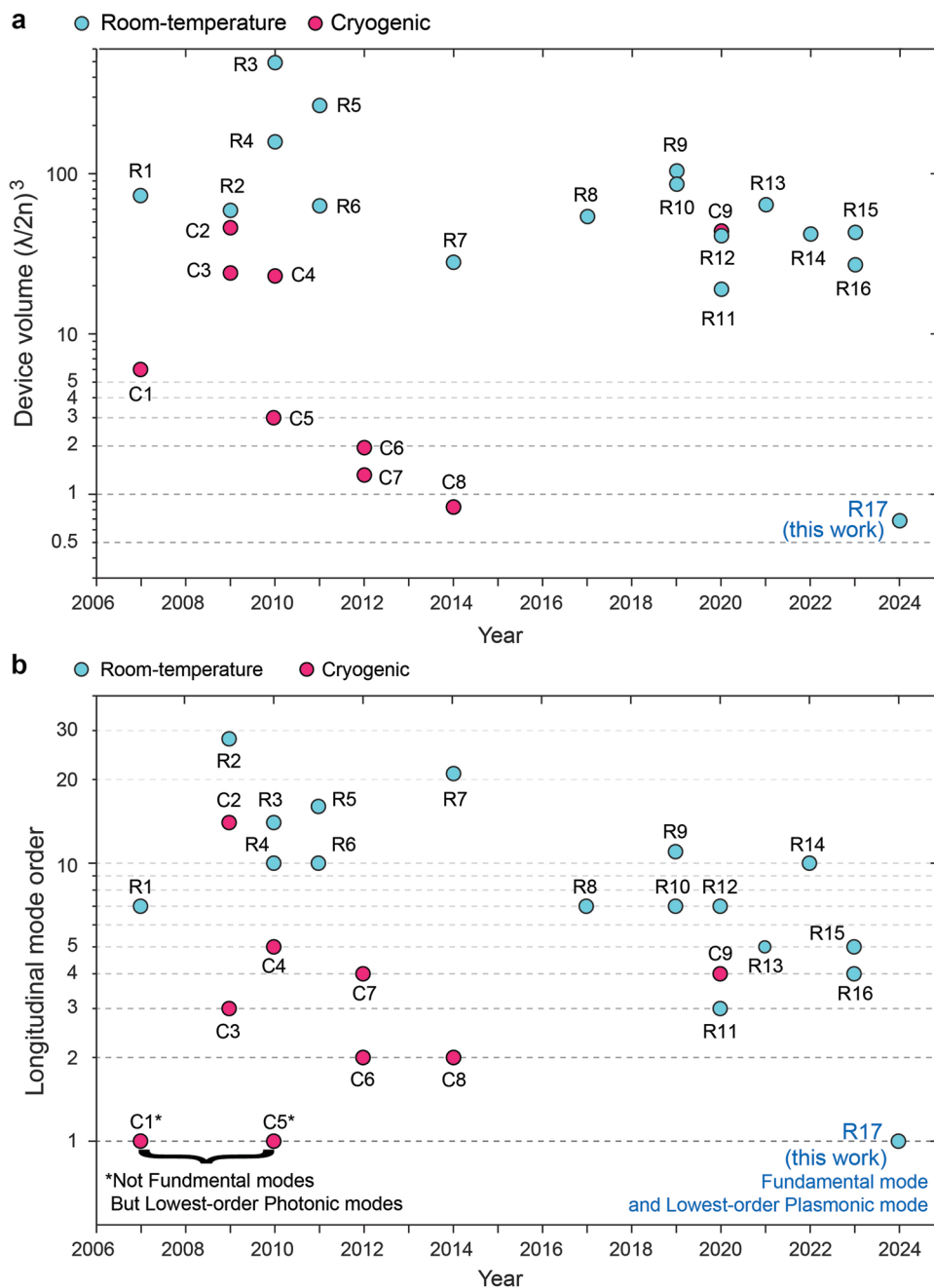
a, Schematic and SEM images of disc-on-pillar array following SiO₂ coating and gold deposition. **b**, Bright-field and SEM images of plasmonic laser particles drop-cast onto a silica-coated silicon substrate, presenting both the III/V side (left) and the Au side (right). **c**, Transmission Electron Microscopy (TEM) image of a cross-section of a sample, prepared using focused ion-beam (FIB) etching.

The image reveals the InGaAsP layer with a thickness of ~290 nm, 5–7 nm thick SiO₂ layer, and ~80-nm thick gold layer. **d**, Higher magnification view of the cross section. **e–f**, Scanning transmission electron microscopy (STEM) images and elemental maps. The samples in **c–f** were prepared by placing the InGaAsP side on a silica-coated silicon substrate and depositing Ga on top of the Au side of the particles. The samples were then placed upside down on a TEM grid.



Extended Data Fig. 9 | Emission spectra of isolated plasmonic LPs. a, SEM image of a semiconductor particle after electron-beam gold deposition. The deposited gold layer appears noticeably rougher than the ‘ultra-flat’ gold substrate shown in Extended Data Fig. 2f. **b,** SEM images of samples with a gold thickness of 100 nm and a side length of 580 nm. **c,** Emission spectra at varying pump fluences. **d,** Light-in-light-out curves measured (circles) along with a

theoretical fit (red curve). **e,** Output spectra of 4 LPs. **f,** Evolution of output spectra of two LPs at pump fluences varying from 0.1 to 4 mJ/cm². The Q factor of the fourth-order longitudinal mode in these devices is estimated to be 42. **g,** SEM images of two samples after gold deposition with a thickness of 15 nm. **h,** Output spectra of two thin-gold-coated samples. The Q factor of the fourth-order mode in these devices is estimated to be approximately 30.



Extended Data Fig. 10 | Device volume and mode order comparison. Device volume (a) and the mode order (b) of single particle and micro- and nano-lasers operating at room temperature (cyan circles) and cryogenic temperature (pink circles). Each data point is labeled with the device name used in Supplementary Tables 1 and 2. Numerous non-metallic lasers based on periodic distributed

feedback, photonic crystal reflection, and lattice structures, which operate in their lowest photonic modes, are not included in this tables since their device sizes exceed multiple wavelengths. Metal-coated lasers in C1 and C5 demonstrate photonic-like modes but do not represent the overall lowest-order plasmonic modes.

Lasing Reporting Summary

Nature Research wishes to improve the reproducibility of the work that we publish. This form is intended for publication with all accepted papers reporting claims of lasing and provides structure for consistency and transparency in reporting. Some list items might not apply to an individual manuscript, but all fields must be completed for clarity.

For further information on Nature Research policies, including our [data availability policy](#), see [Authors & Referees](#).

► Experimental design

Please check: are the following details reported in the manuscript?

1. Threshold

Plots of device output power versus pump power over a wide range of values indicating a clear threshold

Yes
 No

We have quantified the threshold by changing the input pump fluence and measuring the output. The related data is presented in Fig. 2d, Fig. 2i and Extended Data Fig. 8c.

2. Linewidth narrowing

Plots of spectral power density for the emission at pump powers below, around, and above the lasing threshold, indicating a clear linewidth narrowing at threshold

Yes
 No

Linewidth narrowing was observed as the input pump fluence increased. The related data is presented in Fig. 2e and Extended Data Fig. 4.

Resolution of the spectrometer used to make spectral measurements

Yes
 No

We present the spectrometer resolution is 0.8 nm in the methods section.

3. Coherent emission

Measurements of the coherence and/or polarization of the emission

Yes
 No

The spatial coherence of laser light was studied by observing the interference pattern in the scattered layer of Scotch tape (Fig. 4 e–j). The polarization state of the generated laser light was measured. The related data is presented in Extended Data Fig. 3e.

4. Beam spatial profile

Image and/or measurement of the spatial shape and profile of the emission, showing a well-defined beam above threshold

Yes
 No

The laser emission pattern from the $\text{In}_{0.80}\text{Ga}_{0.20}\text{As}_{0.44}\text{P}_{0.56}$ particle at different mode orders was collected by an objective lens and recorded with a silicon-based EMCCD camera, as shown in Fig. 4e–j.

5. Operating conditions

Description of the laser and pumping conditions
Continuous-wave, pulsed, temperature of operation

Yes
 No

Measurement performed under nanoseconds or picoseconds pumping at room condition. We also performed Peltier cooling experiments and the related data was presented in Extended Data Fig. 3d.

Threshold values provided as density values (e.g. W cm^{-2} or J cm^{-2}) taking into account the area of the device

Yes
 No

The threshold value was provide as density value by considering the excitation beam area.

6. Alternative explanations

Reasoning as to why alternative explanations have been ruled out as responsible for the emission characteristics
e.g. amplified spontaneous, directional scattering; modification of fluorescence spectrum by the cavity

Yes
 No

We provided the detailed analysis (Fig. 3 and Extended Data Fig. 5) for the claim of lasing and neglect the other possibilities including modification of fluorescence spectrum by the cavity.

7. Theoretical analysis

Theoretical analysis that ensures that the experimental values measured are realistic and reasonable
e.g. laser threshold, linewidth, cavity gain-loss, efficiency

Yes
 No

We used both semiconductor material modeling, finite difference time domain simulation for studying optical resonance, and a laser rate equation model to analyze the observed laser emission. Please refer to Supplementary Note 1-3 for more details.

8. Statistics

Number of devices fabricated and tested

Yes
 No

We studied more than 120 different particle devices to examine the trend of threshold changes at different sizes (See Fig. 2i). For the half-wavelength laser device, we investigated more than 40 different particles (See Fig. 2c).

Statistical analysis of the device performance and lifetime (time to failure)

- Yes
- No

Statistical analysis and failure of lasing for particle on the dielectric substrate was analyzed and presented in Extended Data Fig 4.